

Numerical study of the sedimentation of spheroidal particles

Mehdi Niazi Ardekani^{a,*}, Pedro Costa^b, Wim Paul Breugem^b, Luca Brandt^a

^a*Linné Flow Centre and SeRC (Swedish e-Science Research Centre), KTH Mechanics, S-100 44 Stockholm, Sweden*

^b*Laboratory for Aero & Hydrodynamics, TU-Delft, Delft, The Netherlands*

Abstract

The gravity-driven motion of rigid particles in a viscous fluid is relevant in many natural and industrial processes, yet this has mainly been investigated for spherical particles. We therefore consider the sedimentation of non-spherical (spheroidal) isolated and particle pairs in a viscous fluid via numerical simulations using the Immersed Boundary Method. The simulations performed here show that the critical Galileo number for the onset of secondary motions decreases as the spheroid aspect ratio departs from 1. Above this critical threshold, oblate particles perform a zigzagging motion whereas prolate particles rotate around the vertical axis while having their broad side facing the falling direction. Instabilities of the vortices in the wake follow when farther increasing the Galileo number. We also study the drafting-kissing-tumbling associated with the settling of particle pairs. We find that the interaction time increases significantly for non-spherical particles and, more interestingly, spheroidal particles are attracted from larger lateral displacements. This has important implications for the estimation of collision kernels and can result in increasing clustering in suspensions of sedimenting spheroids.

Keywords: Non-spherical particles, sedimentation, particle pair interactions, drafting-kissing-tumbling, numerical modelling

*Corresponding author: mehd@mech.kth.se

1. Introduction

The presence of solid rigid particles in a fluid alters the global transport and rheological properties of the mixture in complex and sometimes unpredictable ways. In recent years many efforts have therefore been devoted to develop numerical tools able to fully resolve the fluid-particle and particle-particle interactions and to allow us to investigate rigid particles immersed in an incompressible viscous fluid, see among others [1, 2, 3, 4, 5, 6]. Most of these previous studies consider spherical particles and indeed simulations of suspensions of non-spherical particles are relatively few despite the fact that these are more frequently found. Here we develop a numerical algorithm for spheroidal particles and use it to investigate the sedimentation of isolated and pairs of non-spherical particles. A spheroid, is an ellipsoid with two equal semi-diameters, existing in two shapes of prolate and oblate. For a prolate spheroid the symmetric axis is aligned with the major semi-diameter while for an oblate spheroid this axis is aligned with the minor semi-diameter of the spheroid.

1.1. Sedimentation of isolated spheroids

The gravity-driven motion of heavy particles in a viscous fluid has been a matter of interest among physicists and engineers for decades; it is, however, only recently that the progress in development of computational and experimental techniques has led to a better understanding of the physics behind it.

The simple case of an isolated sphere, fixed in an uniform unbounded flow, has been considered first (see e.g. Johnson & Patel [7]; Ghidersa & Duek [8]; Schouveiler & Provensal [9]; Bouchet et al. [10]). These studies showed different wake structures in different Reynolds number regimes. Allowing the particle to move freely under the effect of gravity introduces new degrees of freedom as path instability can also occur (Jenny et al. [11]; Uhlmann & Dušek [12]). Indeed, these authors reported first the appearance of an oblique wake and then vortex shedding and unsteady motions when increasing the settling speed.

Path and wake instability becomes more complicated in the case of a non-spherical particle as the orientation plays a role in the dynamics of the problem.

Feng et al. (1994) [13] performed two-dimensional numerical simulations of settling elliptic particles and revealed that, in stable conditions, an elliptic particle always falls with its long axis perpendicular to the gravity direction. For three-dimensional oblate particles, the symmetry axis is also aligned with the falling direction in the steady motion at low settling speeds. Increasing the particle size or density, the system becomes unstable and disc-like particles are observed to oscillate horizontally. The ensuing wake instability depends on the aspect ratio and the vortices in the wake are modified as soon as the particle symmetry axis has an angle with respect to the velocity direction, see the review in [14]. The numerical simulations of Mougin & Magnaudet (2001) [15] and Magnaudet & Mougin (2007) [16], considering freely rising and fixed bubbles, revealed that the path instability is closely related to the wake instability. These authors reported a planar zigzagging motion, following a rectilinear path for a frozen oblate bubble with aspect ratio of $\mathcal{AR} = 1/2.5$ (polar over equatorial radius), in agreement with the experimental observations of Ellingsen & Risso (2001) [17]. Unlike the case of sedimenting discs and oblate particles, little is known about prolate particles with finite aspect ratios. This study aims therefore to fill this gap by investigating the sedimentation of isolated prolate and oblate particles in a viscous fluid and comparing the onset and characteristics of the unsteady motion as function of the Galileo number. (The latter quantifies the importance of buoyancy with respect to viscous forces). We find that oblate and prolate particles exhibit different secondary transversal motions with different vortical structures in the unsteady wake. The influence of the aspect ratio on the onset of these unsteady secondary motions is also discussed.

1.2. *Pair interaction between settling spheroids*

Joseph et al. (1987) [18] and Fortes et al. (1987) [19] report a peculiar particle pair interaction for two equal spherical particles. This is the so-called drafting-kissing-tumbling (DKT) phenomenon: it is associated with wake effects and torques acting on two settling particles at sufficiently close vertical distance from each other [13]. The trailing particle is attracted into the wake of the lead-

ing particle, forming a tall body which is unstable and turns. As a consequence, the trailing particle tumbles and falls ahead of that initially leading [20], see the visualization in figure 16. This peculiar interaction has been studied by many both experimentally [13, 19] and numerically [21, 22, 23]. Fornari et al. (2016) [24] performed direct numerical simulations of a suspension of slightly-buoyant spherical particles in a quiescent and turbulent environment. They show that the DKT phenomenon induces a highly intermittent particle velocity distribution which counteracts the reduction of the mean settling velocity caused by the hindered settling effect in a quiescent flow. Pair interactions between settling non-spherical particles has not been studied before, although this is key to understand the collective dynamics of sedimenting non-spherical particles. We therefore examine the DKT of non-spherical particles in the second part of this work. Results of this study reveals that non-spherical particles are attracted towards each other from larger horizontal particle separations and experience a significant increase in the duration of the kissing phase.

1.3. Immersed boundary method (IBM) for non-spherical particles

Among the different approaches proposed to perform interface-resolved direct numerical simulations (DNS) of particle-laden flows, such as *force coupling* [25], *front tracking* [26], *Physalis* [27, 28] and different algorithms based on the *lattice Boltzmann* method for the fluid phase [29, 30], we resort to the *Immersed boundary* method (IBM), which has gained popularity in recent years due to the possibility of using efficient computational methods for solving the Navier-Stokes equations on a Cartesian grid. The IBM was first developed by Peskin (1972) [31] and numerous modifications and improvement have been suggested since then, see [32]. Uhlmann (2005) [33] developed a computationally efficient IBM to fully resolve particle-laden flows. Breugem (2012) [23] improved this method by applying a multi-direct forcing scheme [34] to better approximate the no-slip/no-penetration (ns/np) boundary condition on the surface of the particles and by introducing a slight retraction of the grid points on the surface towards the interior. The numerical stability of the code for mass density ratios (particle

over fluid density ratio) near unity is also improved by a direct account of the inertia of the fluid contained within the particles [35]. In this study the IBM method of Breugem (2012) [23] is extended to ellipsoidal particles. A lubrication correction force based on the asymptotic solution of Jeffrey (1982) [36] is
95 introduced when the gap width between the particles is less than a grid cell and the collision and friction model proposed by Costa et al. [37] employed to calculate the normal and tangential collision forces. To this end, we approximate the interacting objects by two spheres with same mass and radius corresponding to the local curvature at the point of contact.

100 This paper is organised as follows. We discuss the governing equations and the details of the numerical method in section 2, followed by a validation study in section 3. The results of the simulations are discussed in Section 4, first considering isolated particles and then pair interactions. Main conclusions and final remarks are presented in Section 5.

105 2. Governing equations and numerical method

2.1. Governing equations

The motion of rigid ellipsoidal particles is described by the Newton-Euler equations

$$\rho_p V_p \frac{d\mathbf{U}_p}{dt} = \mathbf{F}_p, \quad (1a)$$

$$\frac{d(\mathbf{I}_p \boldsymbol{\omega}_p)}{dt} = \mathbf{T}_p, \quad (1b)$$

where ρ_p , V_p and \mathbf{I}_p are the mass density, volume and moment-of-inertia tensor of a particle. \mathbf{U}_p and $\boldsymbol{\omega}_p$ are the translational and the angular velocity of the particle. The moment of Inertia \mathbf{I}_p of a non-spherical particle changes with the particle orientation and is therefore kept in the time derivative. \mathbf{F}_p and \mathbf{T}_p are the net force and momentum resulting from hydrodynamic stresses on the particle surface, gravity and particle-particle interactions. These can be written

as

$$\mathbf{F}_p = \oint_{\partial V_p} \left[-p\mathbf{I} + \mu_f (\nabla\mathbf{u} + \nabla\mathbf{u}^T) \right] \cdot \mathbf{n} dA - V_p \nabla p_e + (\rho_p - \rho_f) V_p \mathbf{g} + \mathbf{F}_c, \quad (2a)$$

$$\mathbf{T}_p = \oint_{\partial V_p} \mathbf{r} \times \left(\left[-p\mathbf{I} + \mu_f (\nabla\mathbf{u} + \nabla\mathbf{u}^T) \right] \cdot \mathbf{n} \right) dA + \mathbf{T}_c, \quad (2b)$$

where ρ_f is the density of the fluid, \mathbf{g} the gravitational acceleration and \mathbf{r} indicates the distance from the surface to the center of the particle. The stress tensor is integrated over the surface of the particle, denoted ∂V_p . The out-ward pointing unit normal vector at the surface is denoted by \mathbf{n} and the unit tensor by \mathbf{I} . The terms $-\rho_f V_p \mathbf{g}$ and $V_p \nabla p_e$ account for the forces caused by the hydrostatic pressure and a constant pressure gradient ∇p_e or any external force that might be imposed to drive the flow [23]. The force and torque resulting from particle-particle (particle-wall) collisions are indicated by \mathbf{F}_c and \mathbf{T}_c . The fluid velocity \mathbf{u} and the stress tensor $-p\mathbf{I} + \mu_f (\nabla\mathbf{u} + \nabla\mathbf{u}^T)$ appearing in the Newton-Euler equations are obtained from solving the Navier-Stokes and continuity equations

$$\rho_f \left(\frac{\partial \mathbf{u}}{\partial t} + \nabla \cdot \mathbf{u}\mathbf{u} \right) = -\nabla p_e - \nabla p + \mu_f \nabla^2 \mathbf{u} + \rho_f \mathbf{f}, \quad (3a)$$

$$\nabla \cdot \mathbf{u} = 0. \quad (3b)$$

The extra term on the right hand side of the Navier-Stokes equations indicates the IBM force, active in the immediate vicinity of a particle surface to impose indirectly the no-slip / no-penetration (ns/np) boundary condition. In other words, a force distribution \mathbf{f} is imposed on the flow such that the fluid velocity at the surface is equal to the particle surface velocity ($\mathbf{U}_p + \boldsymbol{\omega}_p \times \mathbf{r}$). Eqs. (1) and (3) are coupled through \mathbf{f} and they are solved together.

In the case of spheroidal particles sedimenting in a still fluid examined here, the two non-dimensional parameters defining the problem are the Galileo number and the spheroid aspect ratio. The former is the ratio between gravitational and viscous forces, defined as

$$Ga \equiv \sqrt{\frac{|\rho_p/\rho_f - 1| g D_{eq}^3}{\nu^2}}, \quad (4)$$

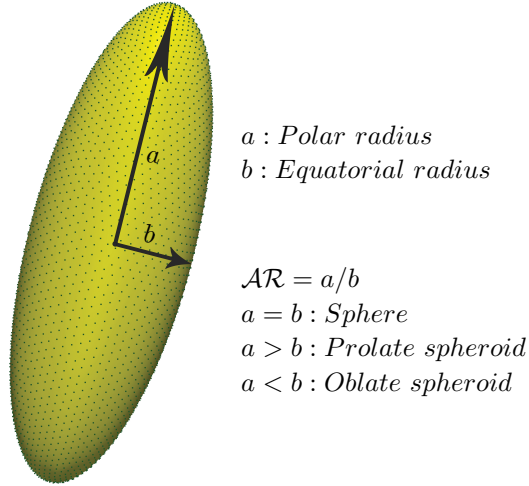


Figure 1: Distribution of the Lagrangian grid points over the surface of a spheroidal particle.

where ρ_p/ρ_f is the particle to fluid density ratio, D_{eq} the diameter of a sphere with the same volume as the ellipsoidal particle. The polar (symmetric semi-
 125 axis) and the equatorial radius, a and b , respectively define the spheroid aspect ratio, $\mathcal{AR} = a/b$ (see figure 1). The results will be presented in terms of the Reynolds number $Re = UL/\nu$, with L and U the characteristic length and velocity scale (typically the particle equivalent diameter D_{eq} and terminal velocity) and ν the kinematic viscosity.

130 *2.2. Numerical method*

2.2.1. Grid geometry

A uniform ($\Delta x = \Delta y = \Delta z$), staggered, Cartesian Eulerian grid is used for the flow and a Lagrangian grid is employed to represent the particles as shown in figure. 1. Uniform distribution of the Lagrangian points over the surface of the particles is obtained by an additional simulation of point charges moving on the surface of the spheroid we wish to simulate. Driven by electrical forces, these charges reach an uniform equilibrium distribution after sufficiently long time. The number of Lagrangian points is defined such that the volume ΔV_l of the Lagrangian grid cells is as close as possible to the volume of the Eulerian

grid cells, Δx^3 . Assuming that the Lagrangian grid corresponds to a thin shell of thickness Δx the number of Lagrangian points can be calculated from

$$N_l = \left[\frac{(a + \Delta x/2)(b + \Delta x/2)^2 - (a - \Delta x/2)(b - \Delta x/2)^2}{3\Delta x^3 / (4\pi)} \right] \quad (5)$$

where a, b are the polar (symmetric semi-axis) and the equatorial radii of the spheroidal particle .

2.2.2. Flow field solution

135 The same *pressure-correction* scheme used in Breugem (2012) [23] is employed to solve the flow field. Equations (3a) and (3b) are integrated in time using an explicit low-storage Runge-Kutta method. A first prediction velocity is used to approximate the IBM force, and a second one to compute the correction pressure and update the pressure field.

140 2.2.3. Solution of the particle motion

Breugem (2012) [23] shows that Eqs. (2) can be re-written in discrete form as as

$$\begin{aligned} \mathbf{U}_p^q = & \mathbf{U}_p^{q-1} - \frac{\Delta t}{V_p} \frac{\rho_f}{\rho_p} \sum_{l=1}^{N_L} \mathbf{F}_l^{q-1/2} \Delta V_l + \frac{1}{V_p} \frac{\rho_f}{\rho_p} \left(\left\{ \int_{V_p} \mathbf{u} dV \right\}^q - \left\{ \int_{V_p} \mathbf{u} dV \right\}^{q-1} \right) \\ & + (\alpha_q + \beta_q) \Delta t \left(1 - \frac{\rho_f}{\rho_p} \right) \mathbf{g} + \left(\frac{\alpha_q + \beta_q}{\rho_p V_p} \right) \Delta t \frac{\mathbf{F}_c^q + \mathbf{F}_c^{q-1}}{2}, \end{aligned} \quad (6)$$

for the linear momentum and

$$\begin{aligned} \mathbf{I}_p^q \boldsymbol{\omega}_p^q = & \mathbf{I}_p^{q-1} \boldsymbol{\omega}_p^{q-1} - \Delta t \rho_f \sum_{l=1}^{N_L} \mathbf{r}_l^{q-1} \times \mathbf{F}_l^{q-1/2} \Delta V_l \\ & + \rho_f \left(\left\{ \int_{V_p} \mathbf{r} \times \mathbf{u} dV \right\}^q - \left\{ \int_{V_p} \mathbf{r} \times \mathbf{u} dV \right\}^{q-1} \right) + (\alpha_q + \beta_q) \Delta t \frac{\mathbf{T}_c^q + \mathbf{T}_c^{q-1}}{2} \end{aligned} \quad (7)$$

for the angular momentum where \mathbf{r} is the position vector, $\mathbf{x} - \mathbf{x}_c$; these are integrated in time with the same Runge-Kutta method used for the flow. $\mathbf{I}_p \boldsymbol{\omega}_p$ is obtained by solving Eq.(7) with the following iterative procedure.

1. As an initial guess \mathbf{I}_p is set equal to the moment-of-inertia tensor at the
145 previous substep \mathbf{I}_p^{q-1} .
2. $\boldsymbol{\omega}_p$ is computed from the linear equations $\mathbf{I}_p \boldsymbol{\omega}_p = \mathbf{B}$, where \mathbf{B} is the right
hand side of eq. (7).
3. The particle rotation during the current substep is indicated by the rota-
tion matrix \mathbf{A} . This is associated to an axis of rotation in the direction of
150 $(\boldsymbol{\omega}_p^q + \boldsymbol{\omega}_p^{q-1})/2$ and an angle of rotation $|(\boldsymbol{\omega}_p^q + \boldsymbol{\omega}_p^{q-1})/2| \cdot (\alpha_q + \beta_q) \cdot \Delta t$.
The rotation matrix is used to update the moment-of-inertia tensor from
the previous substep, $\mathbf{I}_p = \mathbf{A} \mathbf{I}_p^{q-1} \mathbf{A}^{-1}$.
4. The new \mathbf{I}_p is used as initial guess in step 1 until convergence within a
threshold is obtained ($\mathbf{I}_p^{new} - \mathbf{I}_p^{old} < \epsilon$).

This procedure typically requires less than 5 iterations to converge. The orientation of the particle and the position of the Lagrangian points are updated by means of the rotation matrix \mathbf{A} . The position of the particle center and the velocity at the surface of particle are finally computed as

$$\mathbf{x}_c^q = \mathbf{x}_c^{q-1} + \frac{(\alpha_q + \beta_q)}{2} \Delta t (\mathbf{U}_p^q + \mathbf{U}_p^{q-1}), \quad (8a)$$

$$\mathbf{U}(\mathbf{X}_l^q) = \mathbf{U}_p^q + \boldsymbol{\omega}_p \times (\mathbf{X}_l^q - \mathbf{x}_c^q). \quad (8b)$$

155 2.2.4. Lubrication and collision models

Lubrication model.

A particle immersed in a viscous liquid experiences lubrication forces while approaching a wall or another particle. These are due to the film drainage and have an analytical expression in the Stokes regime [38]. The lubrication
160 force is well captured by the IBM method as long as the fluid in the thin gap between the two solid bodies is well resolved. However, for gaps smaller than the Eulerian mesh size, lubrication is under-predicted. To compensate for this inaccuracy and avoid computationally expensive grid refinements, a correction model based on asymptotic expansions of the lubrication force in the Stokes
165 regime is used, see also [37, 39]. Since lubrication is essentially a two-body

problem dominated by the flow in the narrow gap separating two surfaces [40], spheroidal particles are represented as spheres with radius equal to the local radius of curvature of the spheroidal particle. In other words, we approximate the spheroidal particles near contact as spheres with the radius of curvature of the closest points of contact and same mass as the original spheroid and resort to an analytical solution for poly-disperse suspensions of spherical particles [36]. From a computational point of view, the two difficulties are (i) to find the closest points on the surface of the two ellipsoids and (ii) find the local radii of curvature. The efficient iterative method proposed by [41] is employed here to find the closest distance between the two particles. The method can be summarised as follows, see Figure 2 for a visual clarification in 2D.

1. The search algorithm starts from two arbitrary points on the surface of the two particles $(x, y)^k$, assumed initially as the nearest points.
2. Construct two *balls* completely inside the ellipsoids and tangent to the inner surface at the current guess for the nearest points.
3. Find a new guess $(x, y)^{k+1}$ by the intersection of the line of centres $(c_x, c_y)^k$ of the two balls and the surface of the two spheroids.
4. If not converged, go back to step 2. Convergence is obtained when the change of the slope of the line that connects the closest points is below a given threshold.

The procedure converges faster as the radius of the constructed balls increases, however these should fit entirely inside the spheroids.

Once the nearest points are known, the Gaussian radius of curvature R_i is calculated based on the meridional and normal radii of curvature M and N ,

$$M = \frac{a^2 b^2}{\left((a \sin \Phi)^2 + (b \cos \Phi)^2 \right)^{3/2}}, N = \frac{b^2}{\left((a \sin \Phi)^2 + (b \cos \Phi)^2 \right)^{1/2}}. \quad (9)$$

where the semi axes a and b are the polar and the equatorial radius of the spheroid and the angle Φ defines the latitude of the point at which the radius of curvature is being calculated. The Gaussian radius of curvature defines the

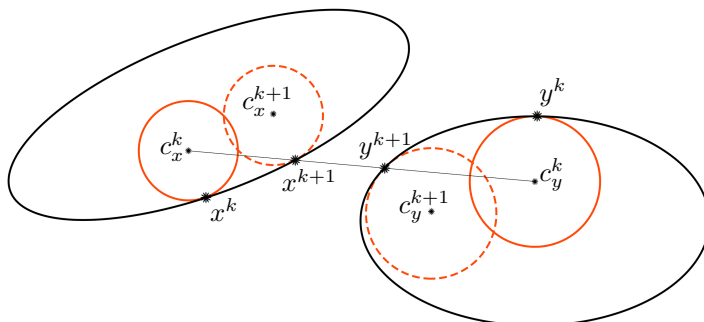


Figure 2: Two-dimensional sketch of the iterative method used to find the nearest distance between two ellipsoids. $(x, y)^k$ are the current guesses for nearest points.

radius of the best fitting sphere tangent to the given surface point

$$R_i = \sqrt{MN} = \frac{a^2 b}{(a \sin \Phi)^2 + (b \cos \Phi)^2}.$$

Note that the best fitting sphere is different from the balls used in the algorithm above and its radius R_i can be larger than a and b .

The lubrication model employed in this study is based on the asymptotic solution of Jeffrey (1982) [36] for spheres with different radii. This two-parameter solution considers normal lubrication effects given by

$$\Delta F_{Lub} = -6\pi\mu R_i \Delta U_n [\lambda(\kappa, \varepsilon) - \lambda(\kappa, \varepsilon_L)], \quad (10)$$

190 where R_i is the radius of curvature, κ the ratio between the radii of curvatures of the two spheres and ε the gap width (closest distance) normalized by the larger radius of curvature. λ is the Stokes amplification factor defined here as in Jeffrey (1982) [36]. ε_L defines the normalized gap width at which the lubrication model becomes active. To account for the presence of surface roughness, and to
 195 limit the lubrication forces to finite values, a threshold width below which the value of the Stokes amplification factor becomes constant ($\varepsilon \leq \varepsilon_r : \lambda(\kappa, \varepsilon) = \lambda(\kappa, \varepsilon_r)$) is introduced. We use here $\varepsilon_L = 0.025$ and $\varepsilon_r = 0.001$ in the case of particle-particle interactions and $\varepsilon_L = 0.05$ and $\varepsilon_r = 0.001$ for particle-wall interactions. A schematic representation of the lubrication model is given in

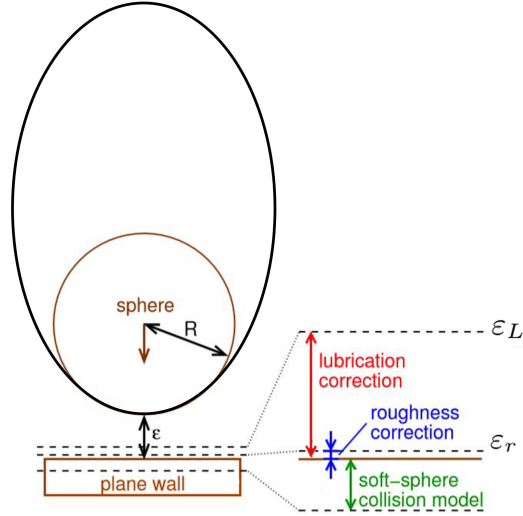


Figure 3: Schematic representation of the lubrication model applied to a sphere approaching a plane wall. A similar approach is used for particle-particle interactions.

200 figure 3. Lubrication corrections responsible for translational and rotational shearing are neglected in this study due to their slower divergence with the gap width: $\Delta F \propto \ln \varepsilon$ versus $\Delta F \propto 1/\varepsilon$ for normal lubrication.

To validate the lubrication model, we compute the normal force between two spheres of different radii ($R_1/R_2 = 1.5$) approaching at equal velocity. Results for the interaction force with and without the lubrication correction are displayed in figure 4 normalized by the Stokes drag in free space (F/F_{sd}). Without correction, the results are in good agreement with the analytical solution of Jeffrey (1982) [36] only when the grid can resolve the flow between the solid objects. For smaller gaps, eq. (10) correctly captures the increase in lubrication.

210 *Collision model.*

When the gap width between two spheroids reduces to zero, the lubrication correction is switched off and a soft sphere collision model [37] activated. To compute the collision forces we proceed as for the lubrication correction model, i.e. the spheroidal particles are approximated as spherical particles with the same mass as the whole particle and with a radius corresponding to the local curvature

215

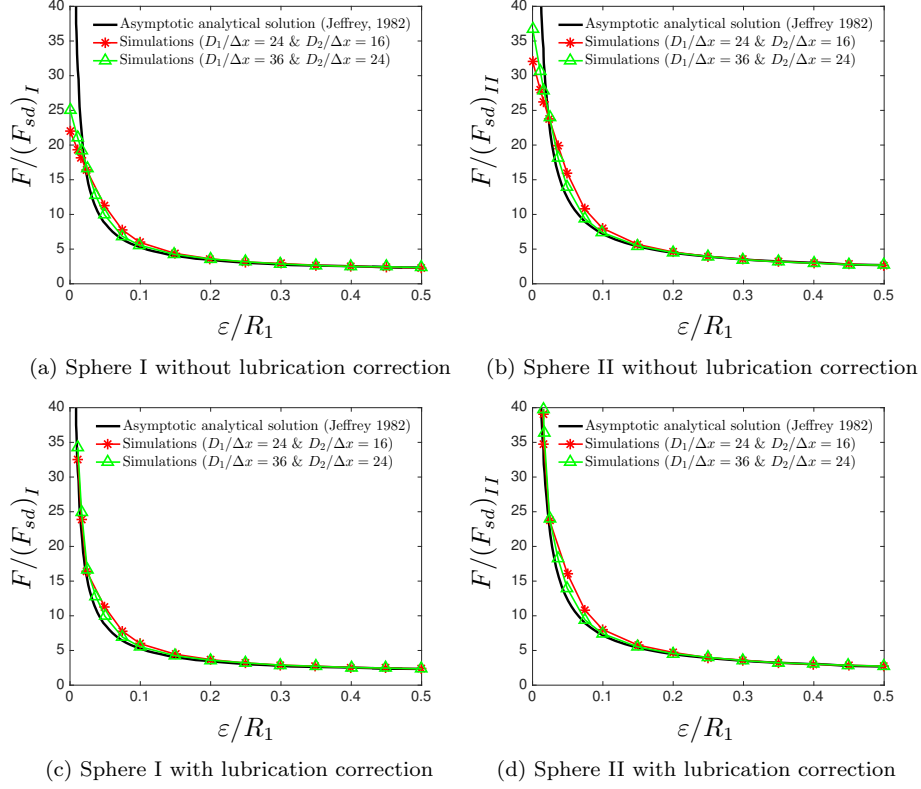


Figure 4: Normal force between two unequal spheres ($R_1/R_2 = 1.5$) approaching at equal velocity with and without lubrication correction for two grid resolutions 24 and 36 grid points per larger diameter, compared to the analytical solution of Jeffrey (1982) [36]. The forces are normalized by the Stokes drag F_{sd} in free space for each particle.

at the contact points. The radii of the approximating spheres remain constant during the collision, simplifying the problem to that of the collision between two unequal spheres. The centres of the approximating colliding spheres are stored at the time step before the gap width becomes negative and updated during the collision using the particle velocity and the rotation matrix introduced above.

220

The soft sphere model used in [37] is employed here to calculate the normal and tangential collision force. In this model, the forces are computed using a linear spring-dashpot system in the normal and tangential directions, with an additional Coulomb friction slider to simulate friction as shown in Figure 5.

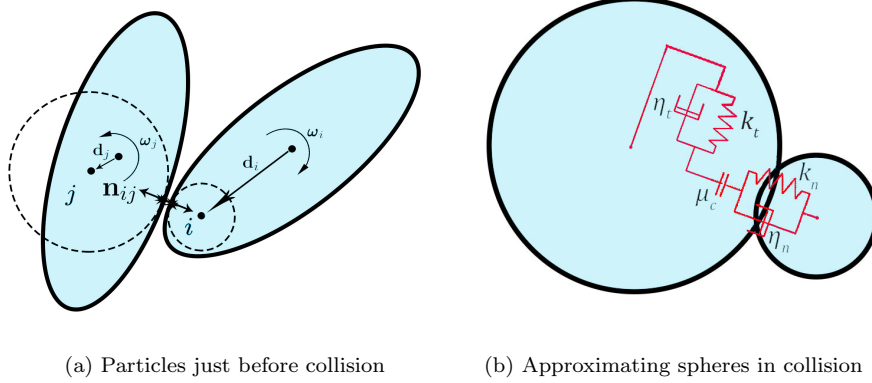


Figure 5: Collision model for spheroidal particles. Sketch of (a) the geometrical and kinetic parameters and (b) the spring-dashpot model used to compute normal and tangential forces.

225 The collision time T is allowed to stretch over N time steps provided that the collision time is still much smaller than the characteristic time scale of the particle motion. This makes the numerical simulation of a wet collision more realistic since the fluid has enough time to adapt to the sudden change in the particle velocity as reported in Costa et al. 2015 [37].

In brief (more details can be found in [37]), the normal collision force depends on the overlap between the two particles and on the normal relative velocity of the surface points located on the line-of-centers. The normal direction \mathbf{n}_{ij} is defined by the vector connecting the centres of the two colliding spheres,

$$\mathbf{n}_{ij} = \frac{\mathbf{x}_j - \mathbf{x}_i}{\|\mathbf{x}_j - \mathbf{x}_i\|}, \quad (11)$$

the penetration as

$$\delta_{ij,n} = (R_i + R_j - \|\mathbf{x}_j - \mathbf{x}_i\|) \mathbf{n}_{ij}, \quad (12)$$

and the normal relative velocity $\mathbf{u}_{ij,n} = (\mathbf{u}_{ij} \cdot \mathbf{n}_{ij}) \mathbf{n}_{ij}$ with

$$\mathbf{u}_{ij} = (\mathbf{u}_i + \boldsymbol{\omega}_i \times \mathbf{d}_i + R_i \boldsymbol{\omega}_i \times \mathbf{n}_{ij}) - (\mathbf{u}_j + \boldsymbol{\omega}_j \times \mathbf{d}_j + R_j \boldsymbol{\omega}_j \times \mathbf{n}_{ji}). \quad (13)$$

where \mathbf{d}_i and \mathbf{d}_j are the vectors that connect the centres of spheroids to the centres of the approximated spheres, while R_i and R_j are the radii of the approximating spheres with centres at \mathbf{x}_i and \mathbf{x}_j . The normal collision force acting

on sphere i when colliding with sphere j is then expressed as

$$\mathbf{F}_{ij,n} = -k_n \boldsymbol{\delta}_{ij,n} - \eta_n \mathbf{u}_{ij,n} \quad (14)$$

with model coefficients

$$k_n = \frac{m_e (\pi^2 + \ln^2 e_{n,d})}{(N\Delta t)^2}, \eta_n = -\frac{2m_e \ln e_{n,d}}{N\Delta t}, m_e = (m_i^{-1} + m_j^{-1})^{-1}. \quad (15)$$

230 k_n and η_n are the normal spring and dashpot coefficients, computed by solving the motion of a linear harmonic oscillator requiring that [42] (i) The magnitude of the normal relative velocity at the end of the collision is equal to the normal restitution coefficient $e_{n,d}$ times the normal velocity at the beginning of the collision. (ii) There is no overlap at the end of the collision ($t = N\Delta t$).

235 The terms m_i and m_j in the expression above are the masses of the spheroidal particles and N is the number of time steps over which the collision is stretched. Large values of N cause a large overlap between particles and therefore an unrealistic delay of the particle rebound, while small values of N result in a lack of accuracy as the collision force may be very large. Here, we use $N = 8$.

The component of the collision force $\mathbf{F}_{ij,t}$ in the tangential direction \mathbf{t}_{ij} is computed similarly with a Coulomb friction included to model the possibility of sliding motion. The tangential force acting on sphere i when colliding with sphere j is expressed as:

$$\mathbf{F}_{ij,t} = \min(\| -k_t \boldsymbol{\delta}_{ij,t} - \eta_t \mathbf{u}_{ij,t} \|, \| -\mu_c \mathbf{F}_{ij,n} \|) \mathbf{t}_{ij}, \quad (16)$$

where the relative tangential velocity $\mathbf{u}_{ij,t} = \mathbf{u}_{ij} - \mathbf{u}_{ij,n}$ and the tangential displacement is denoted $\boldsymbol{\delta}_{ij,t}$. This is computed during the collision by integration of the relative tangential velocity

$$\boldsymbol{\delta}_{ij,t}^{*n+1} = \mathbf{A} \cdot \boldsymbol{\delta}_{ij,t}^n + \int_{t^n}^{t^{n+1}} \mathbf{u}_{ij,t} dt.$$

It should be noted that, to comply with Coulomb's condition, the tangential displacement is saturated when the particles start sliding [43],

$$\boldsymbol{\delta}_{ij,t}^{n+1} = \begin{cases} \boldsymbol{\delta}_{ij,t}^{*n+1} & , \text{ if } \|\mathbf{F}_{ij,t}\| \leq \mu_c \|\mathbf{F}_{ij,n}\|, \\ (1/k_t) (-\mu_c \|\mathbf{F}_{ij,n}\| \mathbf{t}_{ij} - \eta_t \mathbf{u}_{ij,t}) & , \text{ if } \|\mathbf{F}_{ij,t}\| > \mu_c \|\mathbf{F}_{ij,n}\|. \end{cases} \quad (17)$$

The coefficients in Eq. (16) are defined as

$$k_t = \frac{m_{e,t} (\pi^2 + \ln^2 e_{t,d})}{(N\Delta t)^2}, \eta_t = -\frac{2m_{e,t} \ln e_{n,t}}{N\Delta t}, m_{e,t} = (1 + 1/K^2)^{-1} m_e.$$

240 where k_t and η_t are the tangential spring and dashpot coefficients and K is the normalized particle radius of gyration for the approximating spheres ($\sqrt{2/5}$).

The normal and tangential collision forces at the points of contact are finally transferred to the spheroids centres

$$\mathbf{F}_{ij}^c = \mathbf{F}_{ij,n} + \mathbf{F}_{ij,t}, \quad (18a)$$

$$\mathbf{T}_{ij}^c = (\mathbf{d}_i + R_i \mathbf{n}_{ij}) \times \mathbf{F}_{ij,t} + \mathbf{d}_i \times \mathbf{F}_{ij,n}. \quad (18b)$$

2.2.5. Parallelization

The numerical algorithm detailed in the previous subsections is implemented in Fortran with MPI libraries for parallel execution on multi-processor machines with distributed memory. For the parallelization of the Navier–Stokes equations 245 we adopt a standard domain decomposition in two dimensions (streamwise and spanwise) since a 3D parallelization might result in an unbalanced distribution of the computational load among the processors when a preferential direction exists, e.g. in the case of sediments. The particle-related computations follow a master-slave parallelization similar to that used in Breugem (2012) [23]. The 250 processor where the center of a particle is located is denoted as master while the neighbours containing at least one Lagrangian point as slaves. The method requires that a particle fit entirely inside one processor domain, so that it cannot belong to more than 3 slaves. To find the slave neighbors, the ellipsoid is projected in the plane of parallelization. From the equation of the projected ellipse, we compute the intersections with the boundaries of the master domain 255 and thus identify the slave neighbours. The slave processor communicates the data to the master processor, which is the one responsible for the computations of the particle motion.

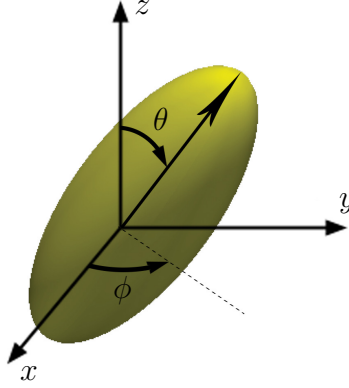


Figure 6: Angles defining the orientation of the spheroid: θ defines the angle between the symmetric axis of the spheroid and the z -axis while ϕ indicates the angle between the projected symmetric axis in the xy plane and the x -axis.

260 3. Validation

3.1. Spheroids in uniform shear flow

The equations of motion of spheroidal particles derived by Jeffery (1922) [44] have been widely used in the literature to track the motion of point particles, particles smaller than the smallest flow scale, at vanishing particle Reynolds number Re_p [45, 46]. Jeffery (1922) [44] also derived the analytical solution for the angular velocities $\dot{\theta}$ and $\dot{\phi}$ in the inertialess regime, $Re_p = 0$, in a simple shear flow,

$$\dot{\theta} = -\frac{G}{a^2 + b^2} (a^2 \cos^2 \theta + b^2 \sin^2 \theta), \quad (19a)$$

$$\dot{\phi} = \frac{G |a^2 - b^2|}{4(a^2 + b^2)} \sin 2\theta \sin 2\phi, \quad (19b)$$

where the semi axes a and b are the polar (symmetric semi-axis) and the equatorial radius of the spheroid, G the imposed shear rate, θ ($0 \leq \theta < \pi$) and ϕ ($0 \leq \phi < 2\pi$) the angles defining the orientation of the spheroid, see figure 6.

In this study, we simulate two spheroids with aspect ratios of $\mathcal{AR} = 2$ and $1/3$ in a plane Couette flow at $Re_p = 0.1$. Re_p is defined by shear rate G and the equivalent particle diameter D_{eq} , i.e. the diameter of a sphere with the same

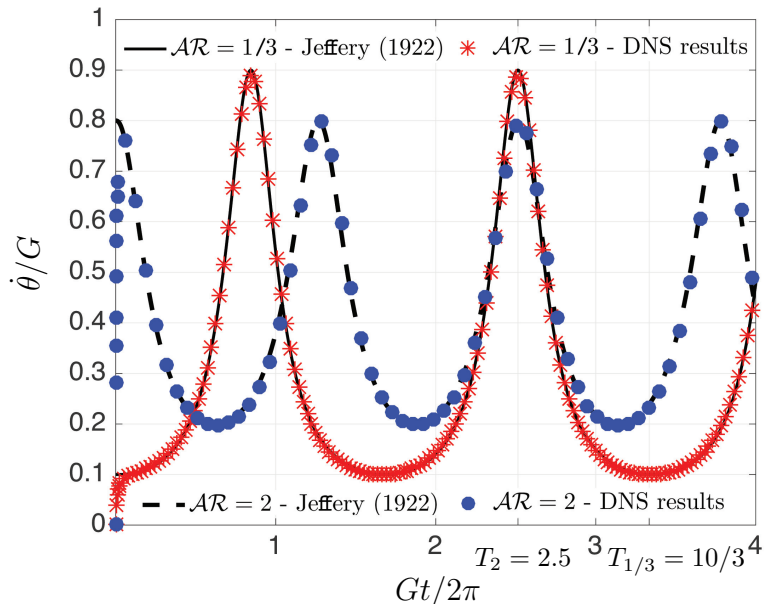


Figure 7: Spanwise component of the angular velocity of spheroids with $\mathcal{AR} = 2$ and $1/3$ against the analytical solution by Jeffery (1922) [44]. Time and angular velocity are non-dimensionalized with $2\pi/G$ and the shear rate G , respectively.

volume of the original spheroid:

$$Re_p \equiv \frac{GD_{eq}^2}{\nu}, D_{eq} = 2(ab^2)^{1/3}. \quad (20)$$

265 Simulations are performed in a domain of size $10D_{eq} \times 10D_{eq} \times 10D_{eq}$ with 32 grid points per D_{eq} and periodic boundary conditions in the direction perpendicular to the velocity gradient. The initial particle orientation is set to $\phi = \theta = 0$ with no initial angular velocity. The particles tumble around the spanwise (normal to the shear plane) axis, as deduced by the analytical solution reported above with
 270 period $T = \frac{2\pi}{G} (\mathcal{AR} + 1/\mathcal{AR})$. The results, shown in figure 7, exhibit excellent agreement with the analytical solution.

3.2. Oblate ellipsoid in cross flow

In this test case, the position of the centre is fixed while the particle is allowed to rotate freely around all three axes. Independent of the initial orientation,

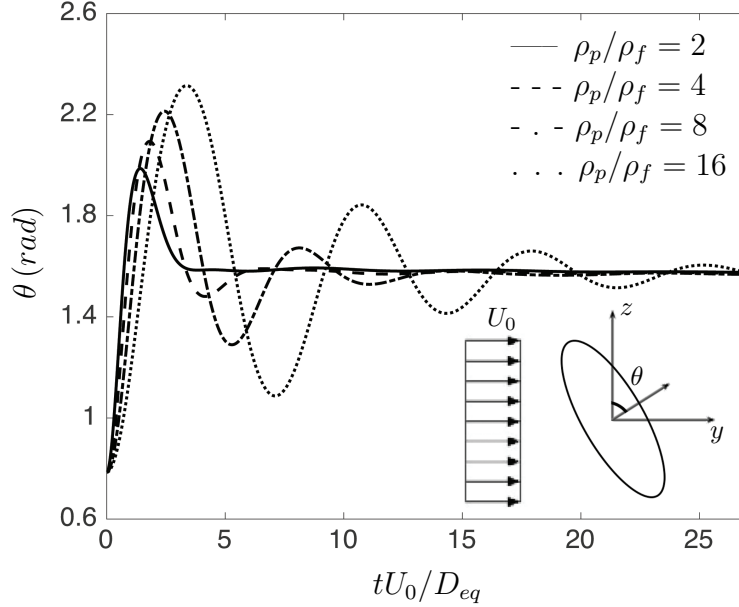


Figure 8: Oscillating oblate in crossflow. Time evolution of the angle ϕ between the particle minor (symmetric) axis and the z axis for different density ratios $\rho_p/\rho_f = 2, 4, 8$ and 16 , $Re_p = 100$ and the aspect ratio $\mathcal{AR} = 1/2.5$.

275 oblate particles align their semi-minor axis with the flow direction. This is consistent with the findings by Feng et al. (1994) [13] that elliptic particles fall with their major axis perpendicular to the gravity direction. As observed by Clift et al. (1978) [47] and Kempe et al. (2009) [48], given an initial deflection, the particle oscillates around one of its major axes (depending on the plane of deflection) and reaches a final equilibrium with its minor axis aligned with the flow. Moreover, by increasing the ratio of particle to fluid density, the period and the magnitude of the oscillations increase.

The simulations are performed here for an oblate particle with $\mathcal{AR} = 1/2.5$ and different density ratios $\rho_p/\rho_f = 2, 4, 8$ and 16 in a numerical domain of $15D_{eq} \times 100D_{eq} \times 15D_{eq}$ in the spanwise x , streamwise y , and wall-normal z directions. The domain is periodic in the wall-parallel directions with two walls moving at same speed in the y direction to create a uniform cross flow.

The resolution is 32 grid point per D_{eq} and the particles Reynolds number, defined by the incoming flow velocity U_0 and the equivalent particle diameter D_{eq} , $Re_p = 100$. The initial deflection $\theta = \pi/4$, with θ the angle between the particle minor (symmetric) axis and the z -axis. The evolution of θ is reported in figure 8 for different density ratios. It is observed, as expected, that the particle reaches an equilibrium with its major axis perpendicular to the flow direction after oscillations of the minor axis around the x -axis. The magnitude of oscillations increases with the density ratio.

4. Results

We study the sedimentation of isolated and particle pairs in a viscous fluid. The results focus on the effect of shape and density ratio on the particle motion.

4.1. Sedimentation of isolated spheroids

The sedimentation of isolated spheroids is simulated in a domain of $15D_{eq} \times 15D_{eq} \times 125D_{eq}$ in the x, y and z directions, with gravity acting in the negative z direction. Periodic boundary conditions are imposed in the horizontal directions whereas a free surface and a rigid wall are used at the upper and bottom boundary. The equivalent particle diameter $D_{eq} = 1.67 \times 10^{-3}m$, corresponding to the diameter of the spherical particles used in the numerical studies of Glowinski et al. (2001) [22], Sharma and Patankar (2005) [49] and Breugem (2012) [23], and water is considered as the fluid. The volume of the particles is kept equal to $(1/6)\pi D_{eq}^3$, while the Galileo number Ga , varied by considering different density ratios (ρ_p/ρ_f) . We investigate spheroids with aspect ratios $\mathcal{AR} = 1/5, 1/3, 1, 3$ and 5 with a resolution of 32 grid points per D_{eq} for all cases except for the particles with aspect ratios $\mathcal{AR} = 1/5$ and 5 where 48 grid points per D_{eq} are used. The resolution is higher than what is typically used for spherical particles [24, 4, 50] to keep an adequate number points per semi-minor axis of the spheroid, which decreases with the aspect ratio. High grid resolution is also needed to capture the flow structures in the unsteady particle wake, especially at the highest settling speed. The spheroidal particle starts falling from

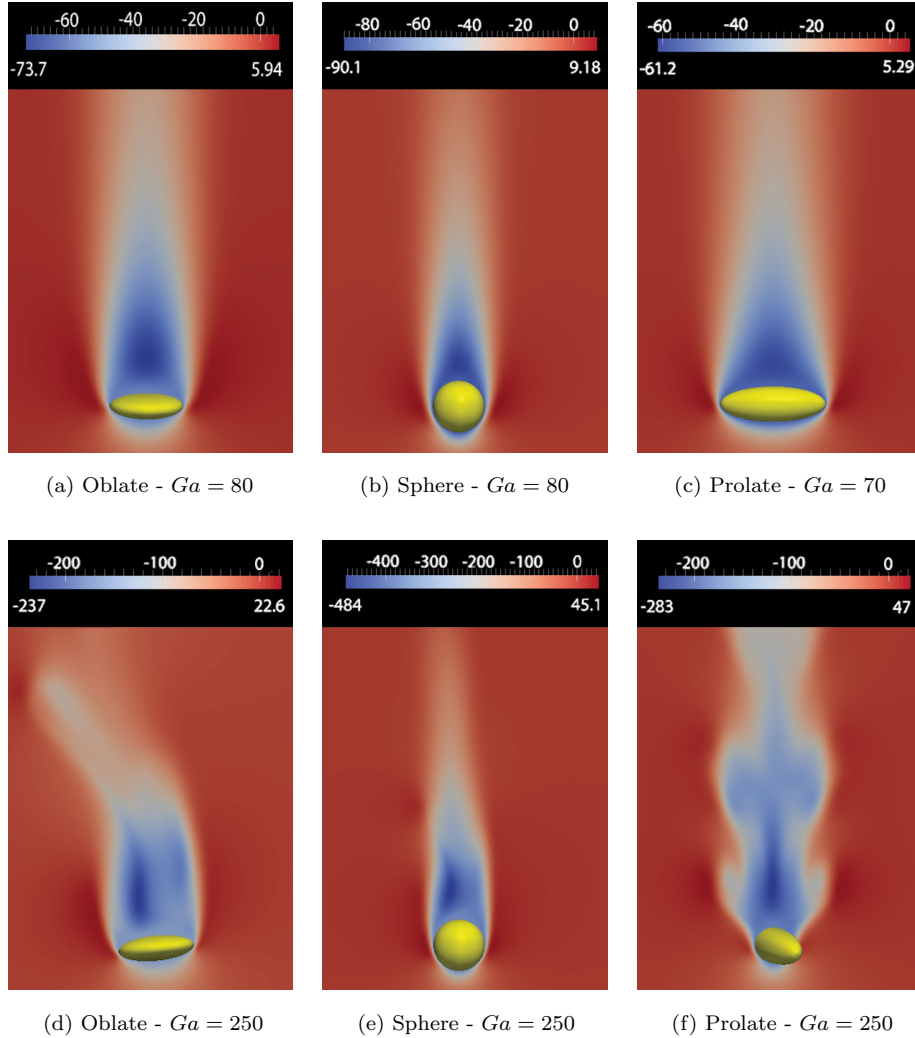


Figure 9: Iso contours of vertical velocity, divided by ν/D_{eq} , for stable and unstable wake behind settling spheroids of aspect ratios $\mathcal{AR} = 1/3, 1$ and 3 . The Galileo number is indicated in each plot.

rest with its major axis perpendicular to the falling direction. This orientation is chosen because other initial orientations are not stable. It is observed here, in agreement with findings in the literature [13, 14], that a spheroidal particle eventually falls with its major axis perpendicular to the gravity direction independent of its initial orientation.

For isolated spheres, the steady-state settling velocity u_t is often expressed in terms of a terminal Reynolds number, $Re_t \equiv u_t D_{eq} / \nu$. Empirical relations can be found in the literature to express Re_t as function of Ga . Yin & Koch (2007) [6], among others, report the drag coefficient for isolated spheres as a function of Re_t , from which the relation between Ga and Re_t can be obtained as shown in Fornari et al. (2016) [24]:

$$Ga^2 = \begin{cases} 18Re_t \left[1 + 0.1315Re_t^{(0.82-0.05 \log Re_t)} \right] & , \text{ if } 0.01 < Re_t \leq 20, \\ 18Re_t \left[1 + 0.1935Re_t^{0.6305} \right] & , \text{ if } 20 < Re_t \leq 260. \end{cases} \quad (21)$$

These relations are used to justify the length of our computational domain in the gravity direction ($125D_{eq}$). Indeed the terminal velocity, Re_t , obtained at $Ga = 80$ and 180 differs by approximately 2% from the predictions using Eqs. (21) ($Re_t = 83$ and 243 , compared to the predicted values of 85 and 248).
325

Jenny et al. (2004) [11] and Uhlmann & Dušek (2014) [12] study the sedimentation of a sphere in a viscous fluid and find four different regimes. Below $Ga \approx 155$ a spherical particle settles steadily on a straight vertical path with an axisymmetric wake consisting of a single toroidal vortex. The wake becomes oblique (with planar symmetry) as the Galileo number increases above 155, and the particle experiences a finite horizontal drift. A pair of thread-like quasi-axial vortices appear in this regime. For Ga from approximately 185 to 215 the particle exhibits periodic oscillations and the wake becomes time-dependent, still preserving the planar symmetry; the wake vortices evolve into a hairpin structure. Finally as Ga further increases, the planar symmetry of the wake is broken and the particle follows a chaotic motion. Our results for spheres are consistent with the findings of [11, 12] and will not be reported here.
330

When considering the settling of isolated spheroids, we observe two different types of unsteady motion, different for oblates and prolates as Ga exceeds the critical threshold for the first bifurcation. Steady and unsteady wakes of spheroids with aspect ratios $\mathcal{AR} = 1/3, 1$ and 3 are depicted in figure 9. The prolate particle rotates around the vertical (z) axis, while the oblate particle performs the so called zigzagging motion [51]. The details of the particle motions when increasing the Galileo number are discussed next for the oblate,
340

345 $\mathcal{AR} = 1/3$, and the prolate particle, $\mathcal{AR} = 3$.

4.1.1. Oblate particles

The oblate particle, $\mathcal{AR} = 1/3$, falls along a straight vertical path with an axisymmetric wake for $Ga \lesssim 130$ (corresponding to $Re_t \approx 103$). For $Ga \gtrsim 130$ the particle path is not vertical anymore, exhibiting an oscillatory motion. 350 Fernandes et al. (2007) [52] report a critical value of $Re_t = 150$ for the onset of oscillatory motion of a circular disc based on the diameter of the disc. Using the major diameter to define Re_t , and not on the equivalent diameter, we obtain a value of 148.5, close to the findings in [52] for discs with same $\mathcal{AR} = 1/3$, and thus an additional validation for our numerical code.

355 As Ga exceeds the critical value of 130, the oblate particle experiences a horizontal drift in a random direction n . For Ga numbers larger than 160, the horizontal velocity soon oscillates around 0, settling into a periodic motion. Interestingly, for Ga numbers between 130 and 160 the oblate particle experiences an oscillation of the drift velocity around a positive value for some significant 360 time interval before initiating the periodic motion. The length of this drift motion decreases in the presence of noise in the flow. The time history of the horizontal velocity V_n is shown in figure 10 for different Ga to document the different transients and the importance of the first shed vortex [14].

A thorough discussion on the oscillatory paths of the disc-like cylinders and 365 oblate spheroids can be found in Ern et al. (2012) [14]. Magnaudet & Mougin (2007)[16] and Yang & Prosperetti (2007)[53] relate the path instability to wake instabilities. We therefore analyze the wake vortices to understand their relation to the particle motion. As shown in figure 11a), initially the wake of an oblate particle consists of a single toroidal vortex, attached to the particle, similar 370 to that of spherical particles in the steady vertical regime. As the instability develops, the particle rotates around one of its major-axes, perpendicular to gravity and to the horizontal direction in which it is drifting. When the angle with respect to the horizontal direction increases, a part of the toroidal vortex detaches forming the head of a hairpin vortex (see figure 11b); this soon develops

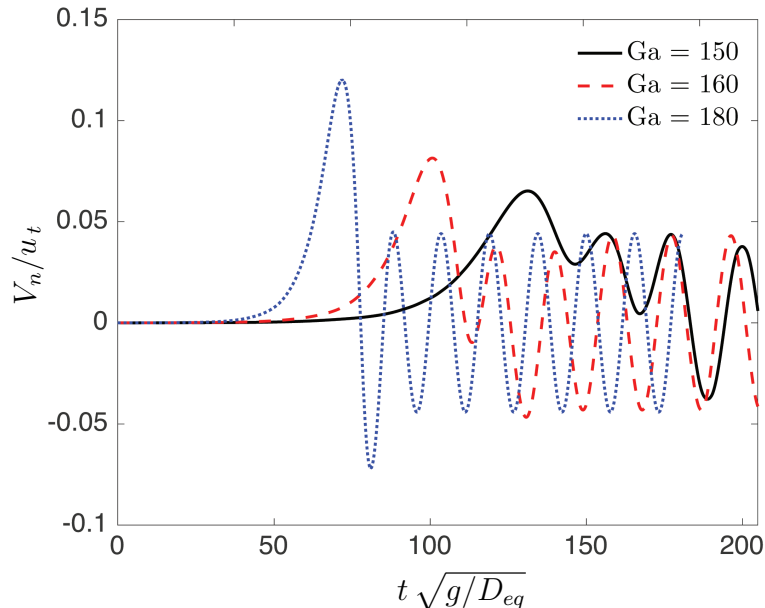


Figure 10: Time history of the horizontal velocity V_n , normalized by the corresponding terminal settling velocity, for an oblate particle of aspect ratio 1/3 and three Galileo numbers, $Ga = 150, 160$ and 180 .

375 further into a full hairpin structure. This vortex pushes the flow near and around
the particle upwards, forming a low pressure region that generates a torque on
the particle in the opposite direction. Owing to inertia, the oblate particle
eventually reaches the opposite inclination. New hairpin vortices then detaches
on the other side and so on each time the particle changes orientation (see
380 figure 11c). The formation of these vortices is also discussed by Auguste et al.
(2010)[54]. For Ga between 130 and 160 the first hairpin vortex detaching is
significantly weaker than those observed for $Ga \gtrsim 160$: the particle does not
change its orientation and continues to drift in the same direction for some time,
see figure 10. This confirms the importance of the strength of the first vortex,
385 as discussed in Ern et al. (2012) [14].

As the oblate particle experiences these oscillations, its vertical velocity de-
creases during the transient, which can be explained by conservation of energy
of the system. Since the first and the second hairpin vortex are the two strongest

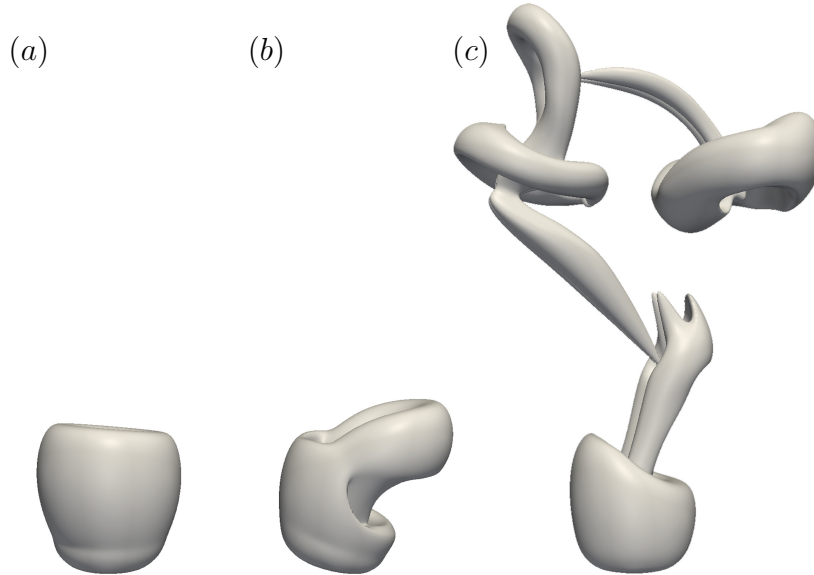


Figure 11: Development of vortices in the wake of an oblate particle with $\mathcal{AR} = 1/3$ and $Ga = 180$. Iso-surfaces of Q-criterion equal to 5% of its maximum are used to identify the vortices.

in terms of their magnitude, the particle experiences two sudden decelerations
 390 before settling to the final regime, characterised by oscillation of its terminal ve-
 locity of the order of 1–2% of its settling speed. The terminal Reynolds number,
 Re_t , based on the averaged settling speed, is depicted for different Ga numbers
 in figure 12 where we also report linear fitting of the data in the steady and un-
 steady regimes. The slope observed in the steady regime ($Ga \lesssim 130$) smoothly
 395 changes and reduces in the unsteady configurations ($Ga \gtrsim 130$). A simple model
 is proposed to predict the terminal Reynolds number for spheroidal particles at
 low Galileo numbers based on the assumption that for oblates, spheres and
 prolate particles the steady flow (wake) regime is similar and only the frontal
 surface area differs. As shown in figure 12 the model provides a good estimate
 400 up till $Ga \approx 130$ where the flow regime is steady and the particle path is vertical.
 The details of the suggested model can be found in appendix A.

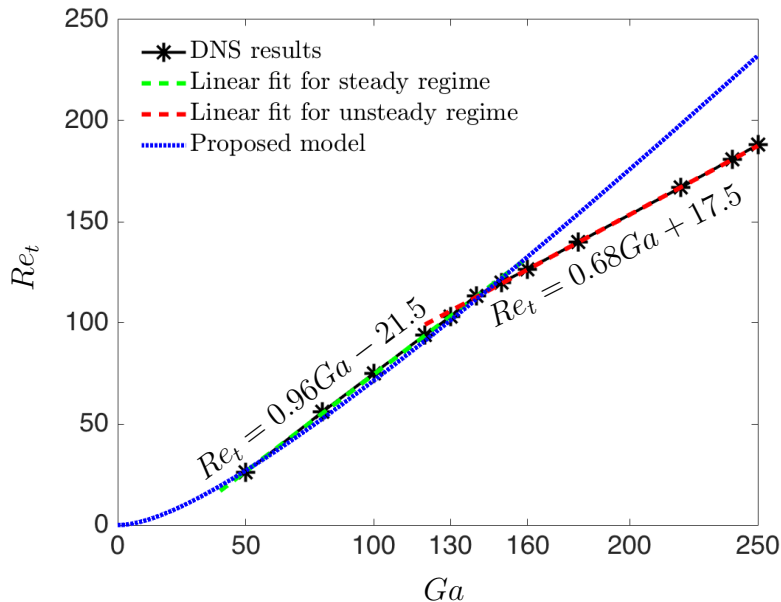


Figure 12: Terminal Reynolds number Re_t , versus Ga for oblate spheroids with $\mathcal{AR} = 1/3$. Linear fitting are also reported for the steady and unsteady regimes. The blue dotted line in the figure indicates the predictions from the proposed model.

4.1.2. Prolate particles

The onset of secondary motions for the prolate particle with $\mathcal{AR} = 3$ is observed at considerably lower Galileo numbers. The settling particle is found to rotate around the vertical direction, z -axis, for Ga exceeding the critical value of 70. The terminal Reynolds number, Re_t , and the z -component of the angular velocity, Ω_z , are depicted in figure 13 as function of Ga . We report here the regime velocities, reached after an initial transient corresponding to a falling distance of about $50 D_{eq}$. The dependence of the terminal velocity on the Galileo number can be approximated by a line for $Ga < 100$, even when the particle undergoes rotation. The slope is found to decrease for $Ga > 100$: here Re_t displays a sudden decrease, which we will explain below by looking at the flow in the particle wake. As for the oblate, assuming the drag depends only on the frontal area fits the data nicely at lower Ga , see appendix A. For $Ga \in [70, 100]$, the angular velocity increases from zero as $\sqrt{Ga - 70}$ before

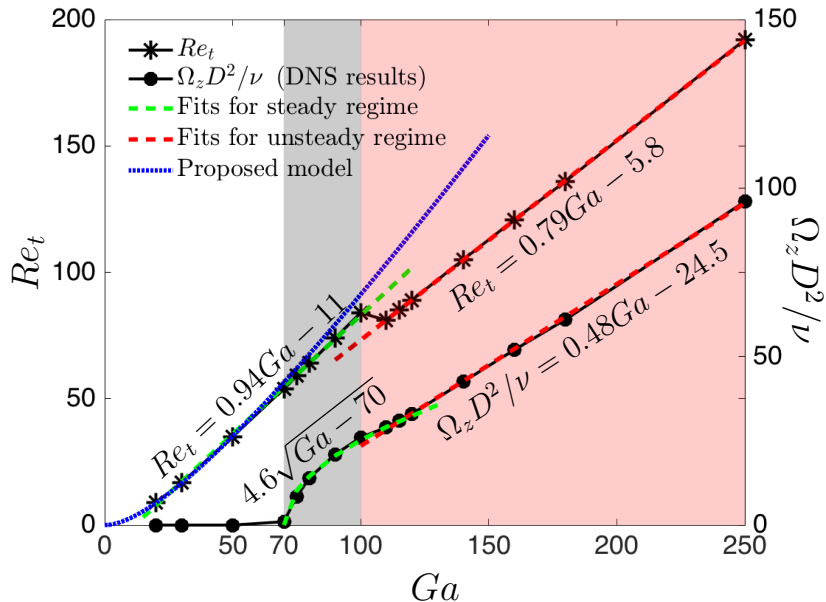


Figure 13: Terminal Reynolds number Re_t and terminal angular velocity Ω_z , divided by ν/D^2 , versus Ga for prolate spheroids with $\mathcal{AR} = 3$. The results of proposed model is shown by the blue dotted line. White background indicates the steady regime, grey refers to the regime where the particle rotates around the vertical axis and the wake consists of four thread-like quasi-axial vortices and pink displays the regime with spiral wake structures (see figure 14).

settling to a linear law as Ga exceeds 100.

To better understand the sudden drop of the vertical and angular velocity at $Ga \approx 100$, we study the structure of the wake behind the prolate particle for the regimes indicated by the different background colours in figure 13. As shown in figure 14 a) the wake is steady and symmetric for $Ga < 70$, consisting of two recirculation regions at the sides. This regime corresponds to the white colour in figure 13. As soon as the particle rotates around the gravity direction four thread-like quasi-axial vortices appear in its wake (figure 14b); these vortices are observed for $70 < Ga < 100$. This regime, indicated by grey colour in figure 13, is very sensitive to external perturbations and indeed any small noise such as the presence of another particle or the vicinity of a wall can

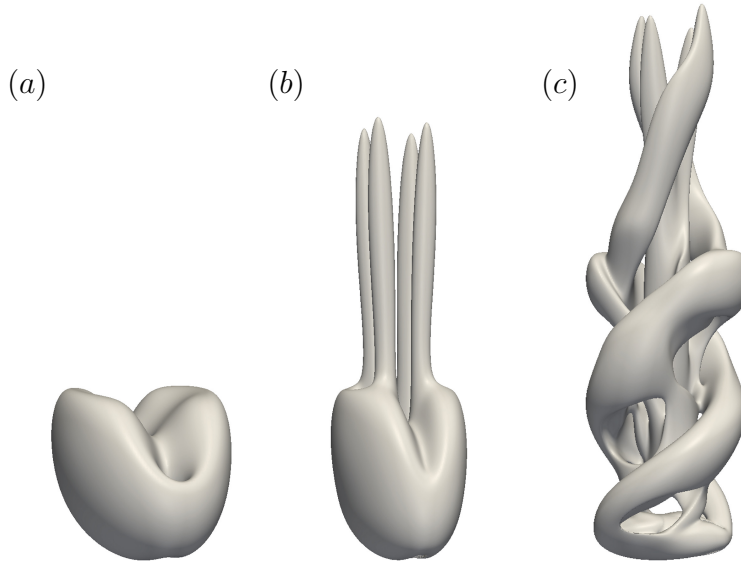


Figure 14: Vortical structures in the wake of a prolate particle with $\mathcal{AR} = 3$ for different Galileo numbers corresponding to the different regimes presented in figure 13. Iso-surfaces of Q -criterion equal to 5% of its maximum are used to identify the vortices at Galileo numbers 60, 80 and 180, respectively.

trigger an instability. This is eventually observed for $Ga > 100$ in the form of helical vortices (see figure 14c representing the flow at $Ga = 180$). The flow kinetic energy increases suddenly when the wake becomes helical, resulting in
 430 the reduction of the particle vertical velocity shown above. The drop in Re_t (cf. figure 13) can therefore be explained by the instability of the vortices in the wake. This occurs at $Ga = 100$ in the simulations presented here, without any additional external noise. As mentioned above, however, the exact value of Ga at which the helical vortices become unstable depends on the ambient noise,
 435 suggesting that we are in the presence of a subcritical instability.

The effect of the particle shape on the terminal velocity and on the onset of secondary motions is also investigated for particles with aspect ratios $\mathcal{AR} = 1/5$ and 5. The terminal Reynolds numbers at $Ga = 80, 180$ and 250 are depicted in figure 15 as function of the spheroid aspect ratio; the Re_t predicted by the
 440 empirical relation in Yin & Koch (2007) [6] for spheres is also indicated in the

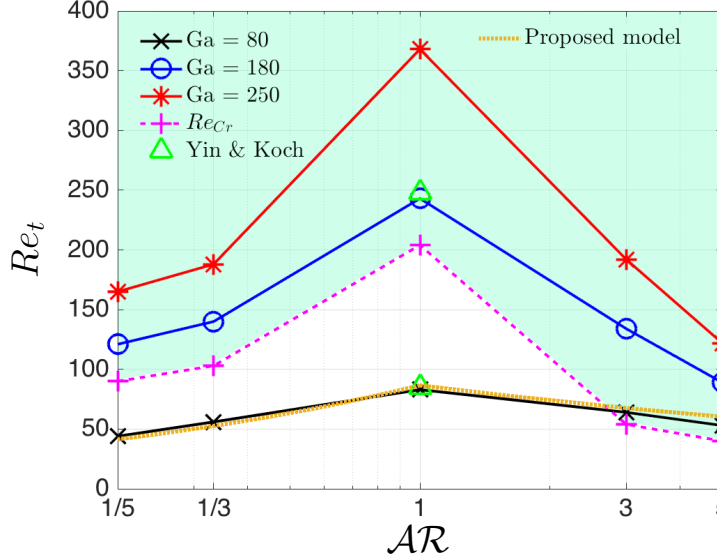


Figure 15: Terminal Reynolds number Re_t , versus the aspect ratio AR for three different Galileo numbers. The region where the particles experience an unsteady motion is indicated by the light green background.

figure for the two lowest Ga . The critical Reynolds number Re_{cr} above which the particles undergo an unsteady motion is determined and indicated by the light green background. Finally, we also report the prediction of the simple model assuming the settling speed can be directly related to the frontal area
445 for $Ga = 80$, when the wake is quasi-steady. We notice good agreement for oblate particles and a slightly lower accuracy for prolate spheroids, which can be explained by the rotational motion they already experience at $Ga = 80$. Spherical particles have the largest settling speed since the sphere corresponds to the object of minimum area perpendicular to the settling direction for a given volume. If the wakes are quasi-steady for all aspect ratios, $Ga = 80$, the
450 minimum cross-section can therefore explain the maximum terminal velocity. This explanation, however, does not hold at higher Ga when the particle motion and the flow become unsteady.

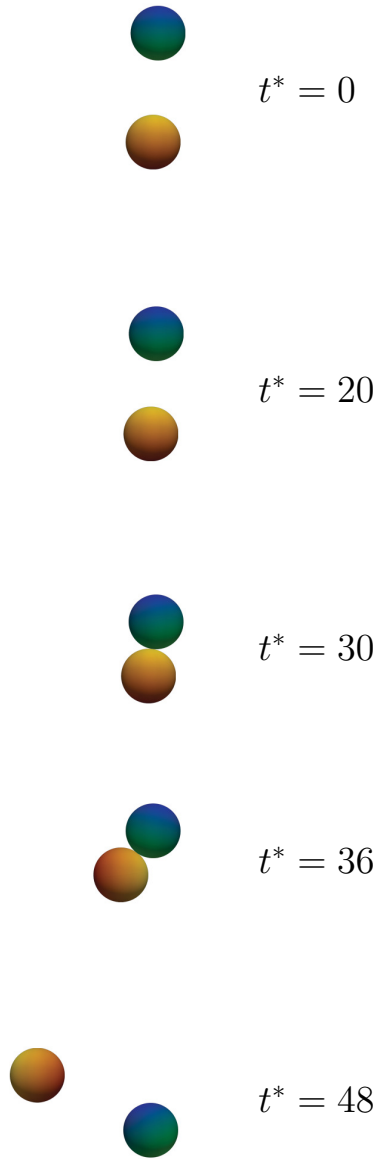


Figure 16: Sequence of Drafting-Kissing-Tumbling (DKT) of two equal spheres from visualizations at non-dimensional times $t^* = 0, 20, 30, 36$ and 48 .

Case	1	1/3	3-0°	3-45°	3-90°
Aspect ratio	1	1/3	3	3	3
Initial orientation of P_1	—	(0, 0, 1)	(1, 0, 0)	(1, 0, 0)	(1, 0, 0)
Initial orientation of P_2	—	(0, 0, 1)	(1, 0, 0)	($\sqrt{2}/2, \sqrt{2}/2, 0$)	(0, 1, 0)

Table 1: Initial orientations of the spheroids at $t^* = 0$ for all studied cases. The orientation vector is defined by the direction of the particle symmetry axis.

4.2. Drafting-Kissing-Tumbling (DKT) of spheroids

Next, we study *Drafting-Kissing-Tumbling* (DKT) of spheroidal particles with different aspect ratios. This peculiar pair interaction has been studied for two equal spheres both experimentally [13, 19] and numerically [23, 22, 21]. The process is reproduced here in figure 16 from our simulations with two equal spheres. The results are reported in non-dimensional time $t^* = t\sqrt{D_{eq}/g}$. Initially, the trailing particle is attracted into the wake of the leading one and drafted towards it with increasing velocity (drafting phase), until they are in contact (kissing phase). The particles in contact form a long body with its major axis parallel to gravity. As discussed previously, this orientation is unstable, as a long body tends to fall with its major axis perpendicular to the falling direction. The two particles therefore tumble [20] (tumbling phase).

We consider now non-spherical particles with the same volume as those in the numerical studies of Glowinski et al. (2001) [22]. Simulations are performed at $Ga = 80$, corresponding to a density ratio of 1.14 and $D_{eq} = 1.67$ mm for spheroids with aspect ratios 1, 3 and 1/3. The corresponding terminal Reynolds number are 83, 64 and 53 respectively, see figure 15.

The two particles start from rest and with their stable orientation (major-axis perpendicular to the falling direction). The initial orientation of the spheroids, defined by the direction of the symmetry axis, are given in table 1 for all 5 cases under investigation. For oblate and spherical particles, the orientation is in the vertical direction whereas it is in the horizontal plane for prolates. Figure 17 shows the initial position and orientation. For prolate particle pairs, among all possible initial conditions, we vary the relative angle between the projection of

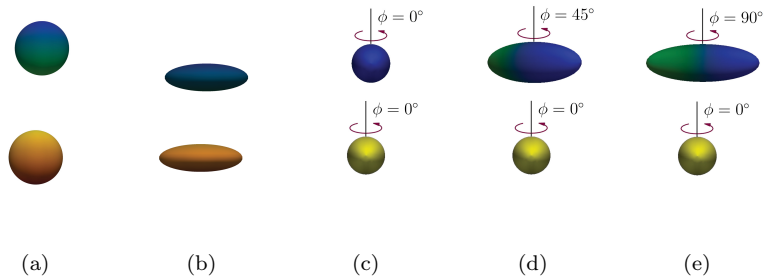


Figure 17: Initial particle configuration for all studied cases a) 1, b) 1/3, c) 3-0°, d) 3-45° and e) 3-90° projected in the $y-z$ plane, with the z parallel to gravity. ϕ is the angle between the symmetric axis of the prolate particle and the x -direction, normal to the page.

the major axis in a plane perpendicular to gravity. Three cases with angles of 0°, 45° and 90° are investigated, see figure 17 c)-e) where colors are used
 480 only for a better visualization. The initial position of the centre of the leading particle, denoted as P_1 , is set to $0.5L_x$, $0.5L_y$ and $0.8L_z$, where L_x , L_y and L_z are the dimensions of the numerical domain. The trailing particle, denoted as P_2 , is above P_1 at a vertical distance between the particle surfaces equal to D_{eq} . An offset of $0.1D_{eq}$ is introduced in the horizontal direction (y -direction for the
 485 sake of clarity) to trigger the DKT [23, 13]. To be able to detect the particle interactions, a relatively high resolution of 48 grid cells per equivalent diameter is chosen. The boundary conditions and the dimensions of the computational domain are those used for a single sedimenting particle, except in the gravity direction where the length is reduced to $L_z = 45D_{eq}$.

490 The time history of the nearest distance between the two settling particles is reported in figure 18: the particle shape indeed alters the DKT and the tumbling disappears in some cases. For the oblate pair and the prolate with 90° angle between the major axes of the two particles, the tumbling phase disappears and the particles continue in contact until they hit the bottom wall. The time
 495 duration of the drafting and kissing phases are listed in table 2 together with the increase of the maximum vertical velocity of the trailing particle with respect to the case of an isolated particle.

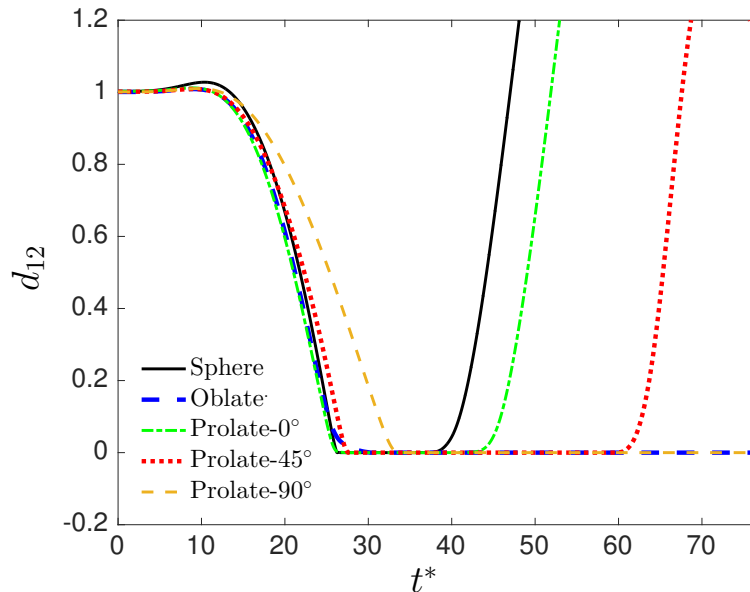


Figure 18: Nearest distance d_{12} between the surfaces of the particle pairs, normalized by the equivalent diameter D_{eq} , versus non-dimensional time t^* for all studied cases.

This increase of the velocity of the trailing particle depends on the overlap with the wake of P_1 . For the cases denoted as 3-0° and 3-90°, the particles
500 preserve the angle between their major axes while drafting. For case the 3-45°, instead, P_2 starts rotating in the drafting phase, reducing the angle between the major axes of the two to about 12°. More details about the secondary motions of the particles are given later in this section. The reduced difference in the velocity of P_2 between cases 3-0° and 3-45° is thus due to the rotation of P_2 ,
505 which reduces the relative angle and increases the overlap with the wake of P_1 ; therefore the two cases are similar in terms of overlap in the drafting phase. The velocity of the leading particle P_1 also increases as P_2 approaches owing to the lubrication forces between the particles. The duration of the drafting phase is the longest for case 3-90° due to the minimum overlap between P_2 and the
510 wake of P_1 . This phase is also relatively long for the oblate case despite of the maximum increased velocity of P_2 ; we attribute this to the lubrication forces

Case	1	1/3	3-0°	3-45°	3-90°
Velocity Increase of P_2	46.68%	51.06%	49.64%	48.19%	31.21%
Drafting period	26.25	30.29	27.32	27.57	33.91
Kissing period	10.16	∞	13.27	30.78	∞

Table 2: Increase of the maximum vertical velocity of the trailing particle, compared to an isolated particle, and time durations of the drafting and kissing phase for the cases considered. The values are reported in non-dimensional time $t^* = t\sqrt{D_{eq}/g}$.

between the oblate particles just before the kissing phase.

Particle pair interactions affects the statistics of settling suspensions in the dilute regime, as shown by the intermittent behaviour reported in [24] for spherical particles. The average vertical velocity of the two particles, normalized by the terminal velocity of an isolated particle, is therefore depicted versus time in figure 19. For spheres, the average of the two particle velocities first increases to ≈ 1.4 and then converges to 1 as the particles starts the tumbling phase, meaning that the interaction between the two does not affect the vertical velocity after the particles move apart from each other. For the prolate particles, cases 3-0° and 3-45°, the average vertical velocity converges to approximately 0.92, lower than the terminal velocity of an isolated prolate particle at $Ga = 80$. This reduction is caused by the change in the wake regime as helical vortices develop in the wake of the two particles, see figure 14c). Interestingly, the average settling speed for the two cases without tumbling, oblate particle pairs and case 3-90°, increases by 49% and 22% respectively.

4.2.1. Oblate particles pairs

We first recall that, unlike spherical particles, settling spheroids can resist horizontal motions by changing the orientation so that their broad-side becomes perpendicular to the velocity direction. They can also be re-oriented by an external torque thus drifting horizontally to balance the horizontal component of the drag force. Figure 20 shows the DK(T, no tumbling in this case) process for oblate particles with aspect ratio $\mathcal{AR} = 1/3$. The corresponding horizontal

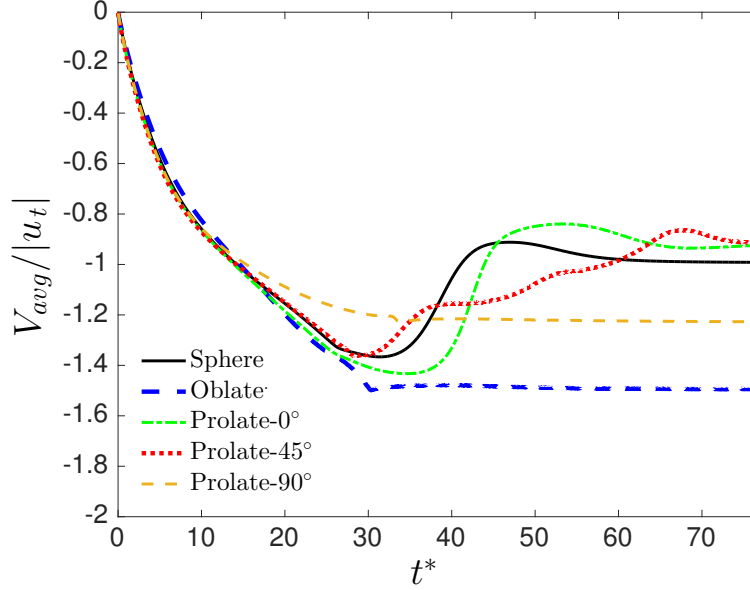


Figure 19: Time evolution of the average vertical velocity of the two particles, normalized by the absolute value of terminal velocity of an isolated particle, for all cases studied.

velocity and inclination, Θ , defined in the yz plane due to the symmetry of
 535 the problem and the initial offset in the y -direction, are given as a function of
 non-dimensional time t^* in figure 21a) and figure 21b).

The trailing particle, P_2 , initially located above and on the right hand side
 of P_1 , experiences a torque originating from the drag difference on its right and
 left side, which results in a small positive y -inclination. With this orientation,
 540 P_2 gains horizontal velocity V_y towards P_1 . This motion forces the leading
 particle to drift in the same direction, to which the particle resists by tilting
 in the direction opposite to that of P_2 , negative Θ in figure 21b ($t^* \approx 10$). As
 a consequence, P_2 moves from the right to the left side of P_1 ; at this point
 ($t^* \approx 25$), the particles experience the same oscillation but in the opposite
 545 direction and with higher lateral velocity and inclination due to the reduced
 distance between the two.

The drafting phase, indicated by the light green background in figure 21,

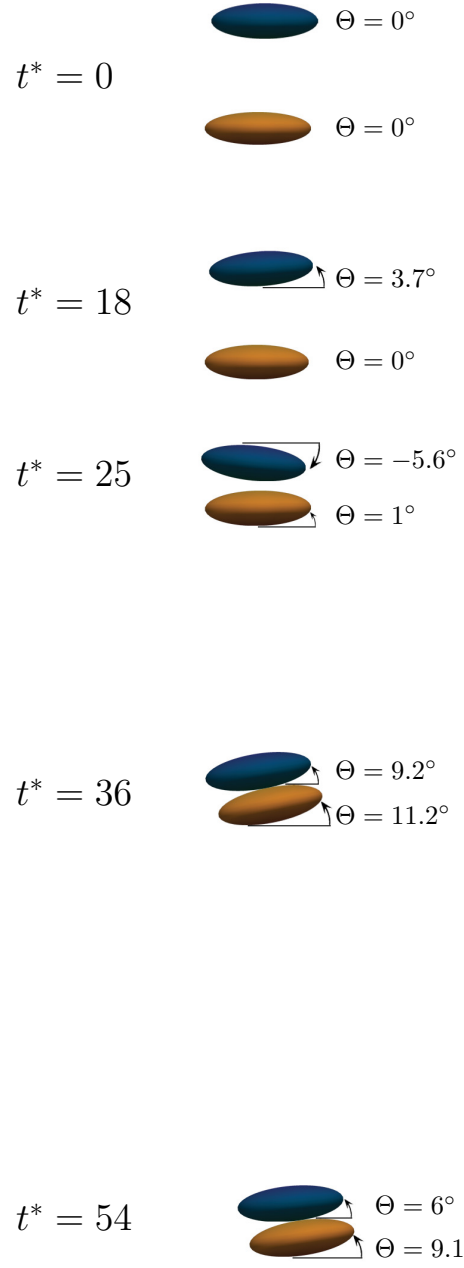


Figure 20: Time sequence of the DKT process for oblate particle pairs with $\mathcal{AR} = 1/3$ and $Ga = 80$ at non-dimensional times $t^* = 0, 18, 25, 36$ and 54 . Θ denotes the angle with respect to the horizontal direction.

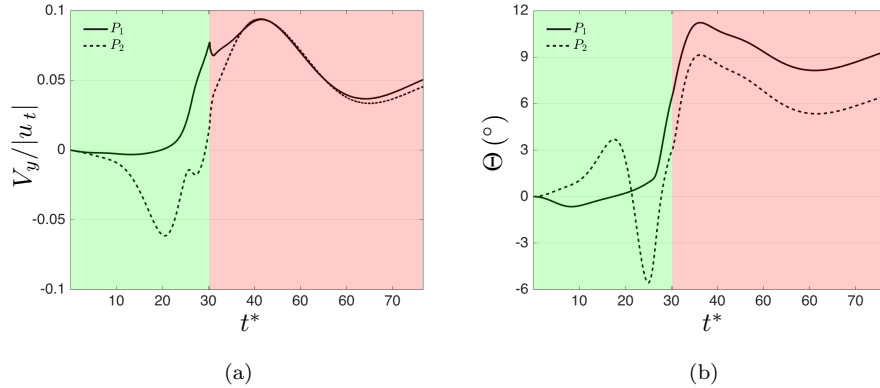


Figure 21: a) The horizontal velocity V_y , normalized by the absolute value of terminal velocity of an isolated case and b) the horizontal (y) inclination angle of the oblate particle pairs with $\mathcal{AR} = 1/3$. The drafting and kissing phase is shown by the light green and the pink background, respectively.

ends as P_2 finally reaches P_1 ($t^* \approx 30$) and the particles fall in contact until they hit the bottom wall. The particles, once in contact, move with a vertical velocity larger than that of an isolated one (≈ 1.5 times), while experiencing two opposite torques that keep them attached and with a positive and nearly constant inclination.

4.2.2. Prolate particle pairs

Prolate particles show different behaviours in the three studied cases; at $Ga = 80$ and for $\mathcal{AR} = 3$ they are in the unstable regime (see figure 13) where their motion and wake structure are sensitive to the interactions with other particles or ambient noise. The sequence of the DKT is displayed in figure 22 for the three cases that we discuss next separately.

Case 3-0° .

In this case the particles are initially parallel, figure 22a, the DKT is analogous to the case of spherical particles, just with a slightly longer duration of the drafting phase and an increase in the duration of the kissing phase of about 30%. The particles start their rotation around the vertical (z) axis in the tumbling phase,

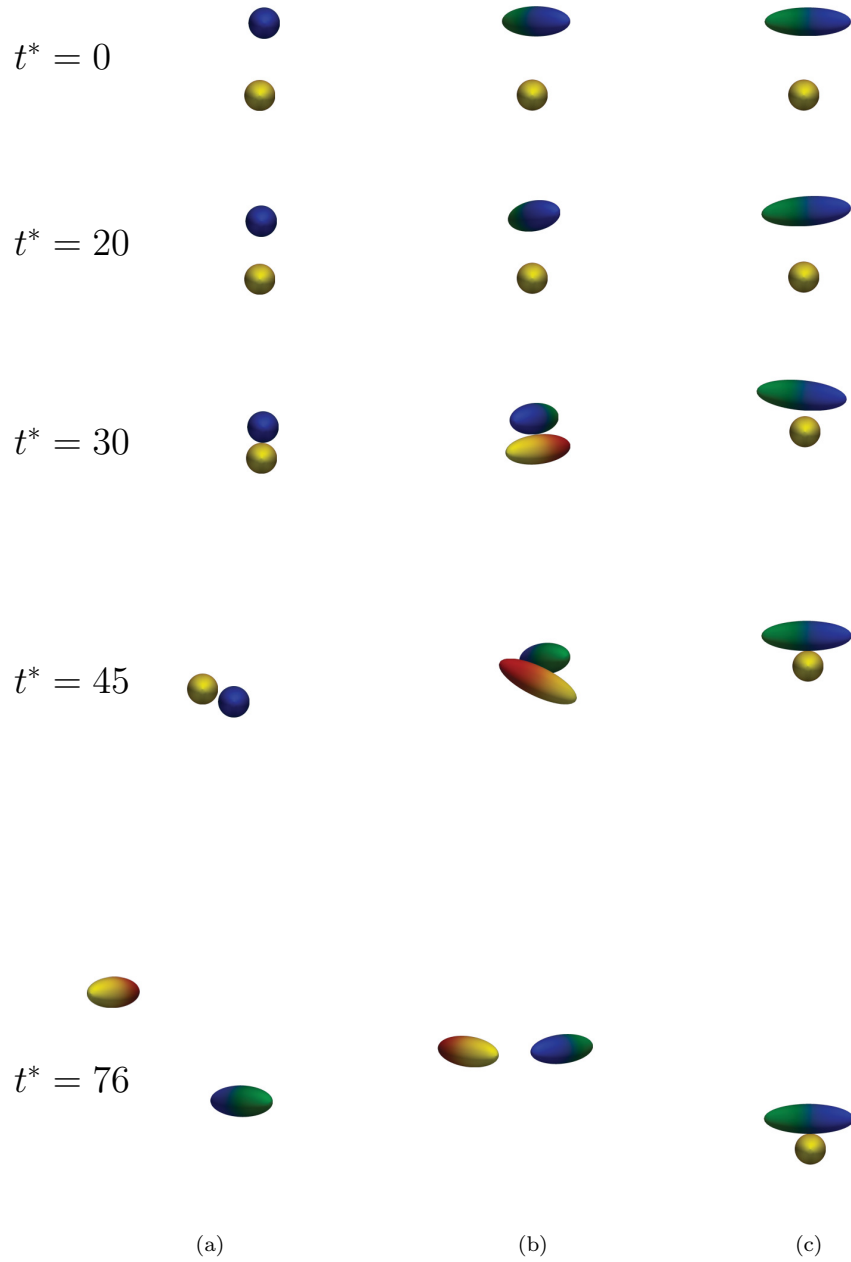


Figure 22: Sequences of a DKT process for prolate particle pairs with $\mathcal{AR} = 3$ in the three cases a) $3-0^\circ$, b) $3-45^\circ$ and c) $3-90^\circ$ at non-dimensional times $t^* = 0, 20, 30, 45$ and 76 .

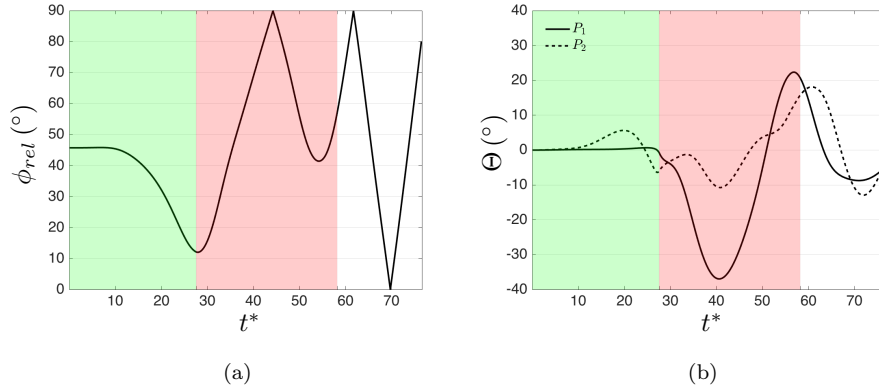


Figure 23: Time history of a) The relative angle ϕ_{rel} between the major axes of the prolate particles in the horizontal plane (xy) and b) the horizontal inclination angle of the prolate particle pair for the case 3-45°. The drafting and kissing phase is shown by the light green and the pink background, respectively.

with helical vortices appearing in their wake. These are triggered by the particle
 565 interactions at Ga less than 100, the critical value for an isolated particle.

Case 3-45° .

In this case, P_2 starts rotating already in the drafting phase, thereby reducing
 the angle between the major axes of the two particles. This is due to the
 torque that P_2 experiences in the low pressure regions behind the poles of P_1 .
 570 Figure 23a reports the relative angle ϕ_{rel} between the major axes of the particles
 in the horizontal xy plane: the relative angle reduces to 12° at the end of drafting
 phase. The motion of P_2 into the wake of P_1 triggers the particle rotation earlier
 than in case 3-0°. The coupled rotation continues in the kissing phase, with a
 duration approximately twice that of two spheres (figure 18); this prevents P_2
 575 from overtaking P_1 in the falling direction. The particles undergo a complex
 rotating motion, with a periodic horizontal inclination, indicated in figure 23b.
 This continues also in the tumbling phase, although with smaller values of the
 inclination angle, Θ . The particle wake is characterised by helical vortices as
 those shown in figure 14 for an isolated prolate. It should be noted here that the
 580 case 3-45° can be taken as a model of the results pertaining larger initial vertical

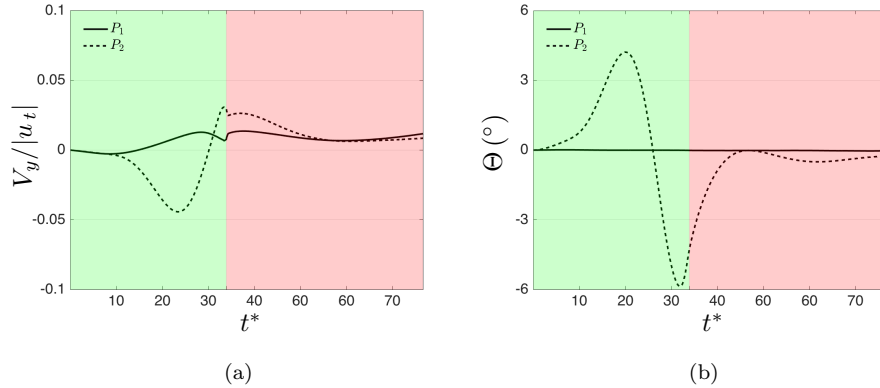


Figure 24: a) Horizontal velocity, V_y normalized by the absolute value of terminal velocity of an isolated particle, and b) the horizontal (y) inclination angle of the prolate particle pair for the case $3\text{-}90^\circ$. The drafting and kissing phase are shown by the light green and the pink background, respectively.

distances between the particles, when the rotating motion might have already begun in the drafting phase and the DKT becomes substantially independent of the initial particle orientation.

Case 3-90° .

585 The DK(T, no tumbling in this case) is similar to the case of oblate particles as P_2 experiences an inclination Θ with respect to the horizontal plane which reduces the initial horizontal offset in the drafting phase, see figure 22c. Figure 24 displays the particle horizontal velocity and inclination in time. P_1 does not experience any tilting due to the symmetry in the x -direction. Thus, P_2

590 is attracted in the wake of P_1 at a lower velocity than in the case of oblate particles. The kissing phase continues until the particles hit the bottom wall, as for $\mathcal{AR} = 1/3$ but without particle oscillation or rotation. The vertical velocity increases by approximately 22% in the kissing phase, and, contrary to our expectations, the particle rotation is delayed until they are about to hit the

595 bottom wall. This observation can be explained by considering the formation of a new body, consisting of the two particles in a cross, which is more stable than an individual prolate particle.

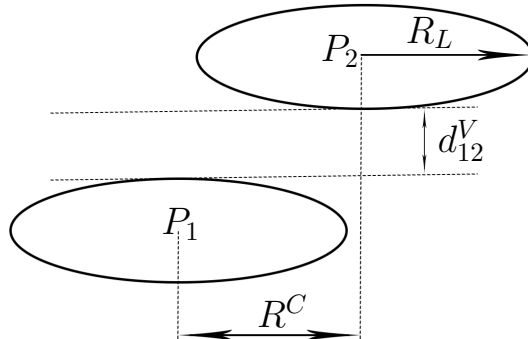


Figure 25: Schematic of initial conditions and parameters measuring the extent of collision.

4.3. The extent of collision domain for two sedimenting spheroids

The results above show that in the case of non-spherical bodies, the trailing
 600 particle P_2 is attracted in the wake of the leading particle P_1 ; the possibility
 to change its orientation gives P_2 an extra horizontal velocity. In turn, P_1 also
 changes its orientation as P_2 approaches.

Motivated by these observations, we speculate that the collision kernels may
 be significantly larger in the case of settling suspensions of non-spherical parti-
 605 cles. An attempt is therefore made to find the initial position from which two
 sedimenting spheroids with the same Galileo number and aspect ratios would
 eventually collide. To reduce the parameter space to be investigated by ex-
 ploiting the symmetry of the problem we shall mainly focus on spherical and
 oblate particles. Indeed, in their stable configuration, these fall axisymmetri-
 610 cally, meaning that we can define on each horizontal plane above the leading
 particle P_1 a circle with centre in P_1 and radius equal to the maximum dis-
 tance to the centre of the trailing particle P_2 such that the two particles will
 collide. The collision between prolate particles, conversely, depends also on the
 initial relative orientation; however for sufficiently long vertical distances and
 615 sufficiently large Ga , the particles rotate along the vertical axis, creating an
 approximate symmetry in the horizontal direction.

The extent of the collision area is computed by considering different vertical
 distances d_{12}^V between the surfaces of the particles and computing the maximum

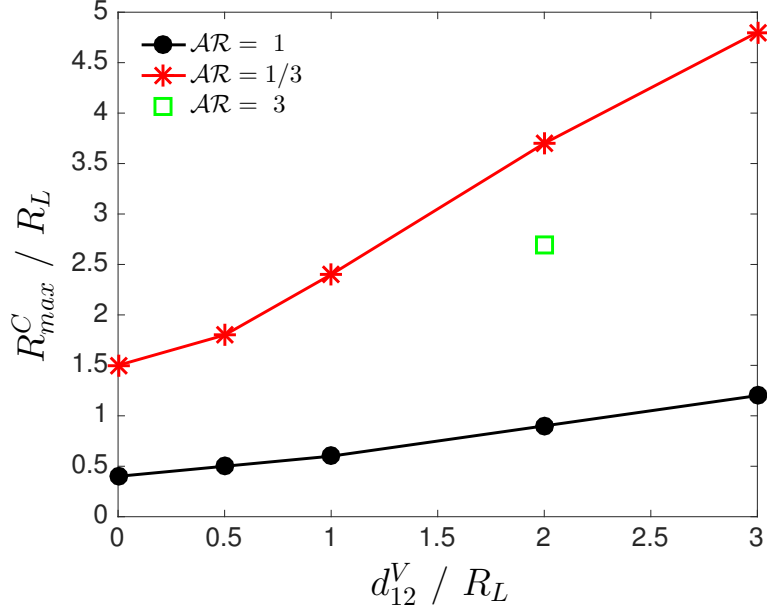


Figure 26: Maximum radius of the collision circle R_{max}^C in the horizontal plane at different vertical distances d_{12}^V between the surfaces of the two particles. The results are normalized here by the larger semi-axis of the spheroids R_L .

horizontal distance between the particle centers for the collision to occur, R_{max}^C .

620 Figure 25 indicates the vertical distance d_{12}^V , the longer semi-axis of the spheroid R_L and the collision radius R^C whose maximum defines the collision area for each vertical distance. For prolate particle pairs the collision area is found for an initial relative angle between the major axis of 45° and a vertical distance $d_{12}^V = 2R_L$ such that they start rotating in the drafting phase. This is to make
625 the outcome less dependent on the initial orientation.

The results are shown in figure 26: each point in the figure is obtained with a series of simulations aiming to identify the occurrence of a collision for each initial vertical distance. The collision domain is a diverging cone: the larger the initial vertical distance, the larger the horizontal distance over which the trailing particle can be attracted. Most importantly, we see that the collision
630 area is considerably larger (up to four times more) for oblate particles than for

spherical ones. The maximum distance for collision, R_{max}^C , is less than $1.5R_L$ for two spheres, meaning that a collision only happens if the particles overlap when projected on the horizontal plane ($d_{12}^H < 2R_L$); R_{max}^C increases to approximately $5R_L$ for oblate particles when the vertical distance between the two particles is $3R_L$. The data point for prolate particles reveals that R_{max}^C is larger than for spheres and lower than for oblate particles.

5. Final remarks

A numerical codes is developed, based on the Immersed Boundary Method, to simulate suspensions of spheroidal particles. The lubrication, collision and friction models used are presented here. These short-range interactions approximate the objects by two spheres with same mass and radius corresponding to the local surface curvature at the points of contact. We use asymptotic analytical expression for the normal lubrication force between unequal spheres and a soft-sphere collision model with coulomb friction. The code is used to investigate the effect of particle shape on the sedimentation of isolated and particle pairs in a viscous fluid. The key observations can be summarised as follows:

- When examining the settling of an isolated particle, we find that the critical Galileo number Ga_{cr} (based on the equivalent sphere diameter D_{eq}) for the onset of secondary motions decreases as the spheroid aspect ratio \mathcal{AR} departs from 1. In particular, the critical Ga decreases more for prolate particles for the same ratio between major and minor axis.
- For $Ga > Ga_{cr}$, oblate particles perform the so called zigzagging motion [51] whereas prolate particles rotate around the vertical (parallel to gravity) axis.
- Different wake regimes are found for prolate particles with $\mathcal{AR} = 3$ (see figures 13 and 14) as we increase Ga . (i) steady axisymmetric wake ($Ga < 70$). (ii) a rotating particle with four thread-like quasi-axial vortices in the wake ($70 < Ga < 100$). (iii) Helical vortices in the wake, associated

660 with a reduction of the vertical velocity ($Ga > 100$). Note that this last bifurcation is found to be sensitive to the level of ambient noise and the value of 100 is obtained with no noise and only 1 particle in the computational domain.

- 665 • We also examine the Drafting-Kissing-Tumbling (DKT) of non-spherical particle pairs at $Ga = 80$, starting with their stable orientation, i.e. the major axis orthogonal to gravity. We find that the tumbling phase disappears in the case of two oblate particles and when the prolates approach each other with their major axes almost orthogonal to each other (figures 16, 20 and 22).
- 670 • In general, for non-spherical bodies, the trailing particle is more promptly attracted (in terms of reducing horizontal distance between the centres) to the wake of the leading particle.
- We determine the volume behind the leading particle inside which the center of trailing particle should be for a collision to occur. This collision domain is found to be considerably larger for oblate particles than 675 for spherical particles. We also consider two prolates at sufficiently long vertical distance so that they rotate in the drafting phase and the results can be seen as less dependent on the initial orientation. The distance at which collisions occur is found to be larger than for spherical particles and 680 lower than oblate.

The results of this study show that sedimenting spheroids are attracted towards each other from longer distances and stay in touch for considerably longer time after they collide than spheres. These two observations suggest that clustering in a suspension of sedimenting spheroids may be significantly larger than 685 for spherical particles. The next step would therefore be to examine collision kernels and clustering of non-spherical particles in quiescent and turbulent environments and how the pair interactions studied here affect the global suspension behaviour.

Acknowledgments

690 This work was supported by the European Research Council Grant No. ERC-2013-CoG-616186, TRITOS. The authors acknowledge computer time provided by SNIC (Swedish National Infrastructure for Computing) and the support from the COST Action MP1305: Flowing matter.

Appendix A. A simple model to predict Re_t for spheroidal particles

695 Here we propose a simple model to predict the terminal Reynolds number Re_t for spheroidal particles at low Galileo numbers. This model assumes that for oblates, spheres and prolate particles the steady flow (wake) regime is similar. In this model the Re -dependent model of Abraham (1970) [55] for perfect sphere is employed to calculate the drag coefficient C_d . The assumption is that for
700 sufficiently small Galileo number, the main effect of a change in spheroid aspect ratio (with respect to a perfect sphere) is the change in the frontal surface area, while C_d remains the same when defining the terminal Reynolds number based on the equivalent sphere diameter:

$$C_d = \left(\sqrt{\frac{24}{Re_t}} + 0.5407 \right)^2 \quad (\text{A.1})$$

The relation between the terminal Reynolds number Re_t , Galileo number
705 Ga and the aspect ratio \mathcal{AR} is given below for oblate and prolate spheroids.

Oblate spheroids.

A simple force balance, using the drag coefficient C_d results in following equations for an oblate spheroid:

$$\frac{1}{2}C_d\pi b^2\rho_f u_t^2 = \frac{1}{6}(\rho_p - \rho_f)\pi D_{eq}^3 g, \quad (\text{A.2})$$

where πb^2 is the projected surface area in direction of gravity when the particle falls with its stable orientation (major-axis perpendicular to the gravity direction), which can be written in term of D_{eq} as

$$\pi b^2 = \frac{1}{4}\pi D_{eq}^2 \mathcal{AR}^{-2/3}. \quad (\text{A.3})$$

Substituting eq. A.3 in A.2 results in a relation between Re_t , Ga and \mathcal{AR} :

$$Re_t^2 + 18.12Re_t^{1.5} + 82.09Re_t - 4.56Ga^2\mathcal{AR}^{2/3} = 0. \quad (\text{A.4})$$

Prolate spheroids.

The same force balance holds for prolate spheroids when the frontal surface area πab , written in terms of D_{eq} as

$$\pi ab = \frac{1}{4}\pi D_{eq}^2 \mathcal{AR}^{1/3}. \quad (\text{A.5})$$

Upon substitution of eq. A.5 in the force balance, the final relation between Re_t , Ga and \mathcal{AR} reads

$$Re_t^2 + 18.12Re_t^{1.5} + 82.09Re_t - 4.56Ga^2\mathcal{AR}^{-1/3} = 0. \quad (\text{A.6})$$

References

References

- [1] K. Yeo, S. Dong, E. Climent, M. Maxey, Modulation of homogeneous turbulence seeded with finite size bubbles or particles, International Journal of Multiphase Flow 36 (3) (2010) 221–233.
- [2] V. Loisel, M. Abbas, O. Masbernat, E. Climent, The effect of neutrally buoyant finite-size particles on channel flows in the laminar-turbulent transition regime, Physics of Fluids (1994-present) 25 (12) (2013) 123304.
- [3] I. Lashgari, F. Picano, W.-P. Breugem, L. Brandt, Laminar, turbulent and inertial shear-thickening regimes in channel flow of neutrally buoyant particle suspensions, Physical review letters 113 (25) (2014) 254502.
- [4] F. Picano, W.-P. Breugem, L. Brandt, Turbulent channel flow of dense suspensions of neutrally-buoyant spheres, Journal of Fluid Mechanics 764 (2015) 463–487.
- [5] I. Lashgari, F. Picano, W.-P. Breugem, L. Brandt, Channel flow of rigid sphere suspensions: particle dynamics in the inertial regime, International Journal of Multiphase Flow 78 (2016) 12–24.

- [6] X. Yin, D. Koch, Hindered settling velocity and microstructure in suspensions of solid spheres with moderate reynolds numbers, *Physics of Fluids* (1994-present) 19 (9) (2007) 093302.
- 725
- [7] T. Johnson, V. Patel, Flow past a sphere up to a reynolds number of 300, *Journal of Fluid Mechanics* 378 (1999) 19–70.
- [8] B. Ghidersa, J. Dušek, Breaking of axisymmetry and onset of unsteadiness in the wake of a sphere, *Journal of Fluid Mechanics* 423 (2000) 33–69.
- [9] L. Schouveiler, M. Provansal, Self-sustained oscillations in the wake of a sphere, *Physics of Fluids* (1994-present) 14 (11) (2002) 3846–3854.
- 730
- [10] G. Bouchet, M. Mebarek, J. Dušek, Hydrodynamic forces acting on a rigid fixed sphere in early transitional regimes, *European Journal of Mechanics-B/Fluids* 25 (3) (2006) 321–336.
- [11] M. Jenny, J. Dušek, G. Bouchet, Instabilities and transition of a sphere falling or ascending freely in a newtonian fluid, *Journal of Fluid Mechanics* 508 (2004) 201–239.
- 735
- [12] M. Uhlmann, J. Dušek, The motion of a single heavy sphere in ambient fluid: a benchmark for interface-resolved particulate flow simulations with significant relative velocities, *International Journal of Multiphase Flow* 59 (2014) 221–243.
- 740
- [13] J. Feng, H. Hu, D. Joseph, Direct simulation of initial value problems for the motion of solid bodies in a newtonian fluid part 1. sedimentation, *Journal of Fluid Mechanics* 261 (1994) 95–134.
- [14] P. Ern, F. Risso, D. Fabre, J. Magnaudet, Wake-induced oscillatory paths of bodies freely rising or falling in fluids, *Annual Review of Fluid Mechanics* 44 (2012) 97–121.
- 745
- [15] G. Mougin, J. Magnaudet, Path instability of a rising bubble, *Physical review letters* 88 (1) (2001) 014502.

- 750 [16] J. Magnaudet, G. Mougin, Wake instability of a fixed spheroidal bubble, *Journal of Fluid Mechanics* 572 (2007) 311–337.
- [17] K. Ellingsen, F. Risso, On the rise of an ellipsoidal bubble in water: oscillatory paths and liquid-induced velocity, *Journal of Fluid Mechanics* 440 (2001) 235–268.
- 755 [18] D. Joseph, A. Fortes, T. Lundgren, P. Singh, Nonlinear mechanics of fluidization of beds of spheres, cylinders and disks in water, *Advances in Multiphase Flow and Related Problems* (1987) 101–122.
- [19] A. Fortes, D. Joseph, T. Lundgren, Nonlinear mechanics of fluidization of beds of spherical particles, *Journal of Fluid Mechanics* 177 (1987) 467–483.
- 760 [20] A. Prosperetti, G. Tryggvason, *Computational methods for multiphase flow*, Cambridge university press, 2007.
- [21] N. Patankar, P. Singh, D. Joseph, R. Glowinski, T. Pan, A new formulation of the distributed lagrange multiplier/fictitious domain method for particulate flows, *International Journal of Multiphase Flow* 26 (9) (2000) 1509–1524.
- 765 [22] R. Glowinski, T. Pan, T. Hesla, D. Joseph, J. Periaux, A fictitious domain approach to the direct numerical simulation of incompressible viscous flow past moving rigid bodies: application to particulate flow, *Journal of Computational Physics* 169 (2) (2001) 363–426.
- 770 [23] W.-P. Breugem, A second-order accurate immersed boundary method for fully resolved simulations of particle-laden flows, *Journal of Computational Physics* 231 (13) (2012) 4469–4498.
- [24] W. Fornari, F. Picano, L. Brandt, Sedimentation of finite-size spheres in quiescent and turbulent environments, *Journal of Fluid Mechanics* 788 (2016) 640–669.
- 775

- [25] S. Lomholt, M. Maxey, Force-coupling method for particulate two-phase flow: Stokes flow, *Journal of Computational Physics* 184 (2) (2003) 381–405.
- [26] S. Unverdi, G. Tryggvason, A front-tracking method for viscous, incompressible, multi-fluid flows, *Journal of computational physics* 100 (1) (1992) 25–37.
- [27] A. Sierakowski, A. Prosperetti, Resolved-particle simulation by the physalis method: Enhancements and new capabilities, *Journal of Computational Physics* 309 (2016) 164–184.
- [28] Z. Zhang, A. Prosperetti, A second-order method for three-dimensional particle simulation, *Journal of Computational Physics* 210 (1) (2005) 292–324.
- [29] A. J. Ladd, Numerical simulations of particulate suspensions via a discretized boltzmann equation. part 1. theoretical foundation, *Journal of Fluid Mechanics* 271 (1994) 285–309.
- [30] A. J. Ladd, Numerical simulations of particulate suspensions via a discretized boltzmann equation. part 2. numerical results, *Journal of Fluid Mechanics* 271 (1994) 311–339.
- [31] C. Peskin, Flow patterns around heart valves: a numerical method, *Journal of computational physics* 10 (2) (1972) 252–271.
- [32] R. Mittal, G. Iaccarino, Immersed boundary methods, *Annual Review of Fluid Mechanics* 37 (2005) 239–261.
- [33] M. Uhlmann, An immersed boundary method with direct forcing for simulation of particulate flow, *Journal of Computational Physics* 209 (2) (2005) 448–476.
- [34] K. Luo, Z. Wang, J. Fan, K. Cen, Full-scale solutions to particle-laden flows: Multidirect forcing and immersed boundary method, *Physical Review E* 76 (6) (2007) 066709.

- [35] T. Kempe, J. Fröhlich, An improved immersed boundary method with
805 direct forcing for the simulation of particle laden flows, *Journal of Computational Physics* 231 (9) (2012) 3663–3684.
- [36] D. Jeffrey, Low-reynolds-number flow between converging spheres, *Journal of Fluid Mechanics*.
- [37] P. Costa, B. Boersma, J. Westerweel, W.-P. Breugem, Collision model for
810 fully resolved simulations of flows laden with finite-size particles, *Physical Review E* 92 (5) (2015) 053012.
- [38] H. Brenner, The slow motion of a sphere through a viscous fluid towards a plane surface, *Chemical engineering science* 16 (3) (1961) 242–251.
- [39] W.-P. Breugem, A combined soft-sphere collision/immersed boundary
815 method for resolved simulations of particulate flows, in: *ASME 2010 3rd Joint US-European Fluids Engineering Summer Meeting collocated with 8th International Conference on Nanochannels, Microchannels, and Minichannels*, American Society of Mechanical Engineers, 2010, pp. 2381–2392.
- [40] I. Claeys, J. Brady, Suspensions of prolate spheroids in stokes flow. part 1. dynamics of a finite number of particles in an unbounded fluid, *Journal of Fluid Mechanics* 251 (1993) 411–442.
- [41] A. Lin, S.-P. Han, On the distance between two ellipsoids, *SIAM Journal on Optimization* 13 (1) (2002) 298–308.
- [42] M. Van Der Hoef, M. Van Sint Annaland, J. Kuipers, Computational fluid
825 dynamics for dense gas–solid fluidized beds: a multi-scale modeling strategy, *Chemical Engineering Science* 59 (22) (2004) 5157–5165.
- [43] S. Luding, Introduction to discrete element methods: basic of contact force models and how to perform the micro-macro transition to continuum theory, *European Journal of Environmental and Civil Engineering* 12 (7-8)
830 (2008) 785–826.

- [44] G. Jeffery, The motion of ellipsoidal particles immersed in a viscous fluid, in: Proceedings of the Royal Society of London A: Mathematical, Physical and Engineering Sciences, Vol. 102,715, The Royal Society, 1922, pp. 161–179.
- 835
- [45] L. Zhao, C. Marchioli, H. Andersson, Slip velocity of rigid fibers in turbulent channel flow, *Physics of Fluids (1994-present)* 26 (6) (2014) 063302.
- [46] C. Marchioli, A. Soldati, Rotation statistics of fibers in wall shear turbulence, *Acta Mechanica* 224 (10) (2013) 2311–2329.
- 840 [47] R. Clift, J. Grace, M. Weber, Bubbles, drops, and particles, Courier Corporation, 2005.
- [48] T. Kempe, S. Schwarz, J. Fröhlich, Modelling of spheroidal particles in viscous flows, in: Proceedings of the Academy Colloquium Immersed Boundary Methods: Current Status and Future Research Directions (KNAW, Amsterdam, The Netherlands, 15–17 June 2009), 2009.
- 845
- [49] N. Sharma, N. Patankar, A fast computation technique for the direct numerical simulation of rigid particulate flows, *Journal of Computational Physics* 205 (2) (2005) 439–457.
- [50] M. Uhlmann, T. Doychev, Sedimentation of a dilute suspension of rigid spheres at intermediate galileo numbers: the effect of clustering upon the particle motion, *Journal of Fluid Mechanics* 752 (2014) 310–348.
- 850
- [51] G. Mougin, J. Magnaudet, Wake-induced forces and torques on a zigzagging/spiralling bubble, *Journal of Fluid Mechanics* 567 (00) (2006) 185–194.
- [52] P. Fernandes, F. Risso, P. Ern, J. Magnaudet, Oscillatory motion and wake instability of freely rising axisymmetric bodies, *Journal of Fluid Mechanics* 573 (2007) 479–502.
- 855
- [53] B. Yang, A. Prosperetti, Linear stability of the flow past a spheroidal bubble, *Journal of Fluid Mechanics* 582 (2007) 53–78.

- 860 [54] F. Auguste, D. Fabre, J. Magnaudet, Bifurcations in the wake of a thick circular disk, *Theoretical and Computational Fluid Dynamics* 24 (1-4) (2010) 305–313.
- [55] F. Abraham, Functional dependence of drag coefficient of a sphere on reynolds number, *Physics of fluids* 13 (1970) 2194–2195.